



1 Mountain permafrost in the Central Pyrenees: insights from  
2 the Devaux ice cave

3 Miguel Bartolomé<sup>1\*</sup>, Gérard Cazenave<sup>2</sup>, Marc Luetscher<sup>3</sup>, Christoph Spötl<sup>4</sup>,  
4 Fernando Gázquez<sup>5,6</sup>, Ánchel Belmonte<sup>7</sup>, Alexandra V. Turchyn<sup>8</sup>, Juan Ignacio  
5 López-Moreno<sup>1</sup>, Ana Moreno<sup>1</sup>

6 1 Departamento de Procesos Geoambientales y Cambio Global, Instituto  
7 Pirenaico de Ecología-CSIC, Zaragoza, Spain.

8 2 Société de Spéléologie et de Préhistoire des Pyrénées Occidentales  
9 (SSPPO), 5 allée du Grand Tour, 64000 PAU, France

10 3 Swiss Institute for Speleology and Karst Studies (SISKA), La Chaux-de-  
11 Fonds, Switzerland

12

13 4 Institute of Geology, University of Innsbruck, 6020 Innsbruck, Austria

14 5 Water Resources and Environmental Geology Research Group, Department  
15 of Biology and Geology, University of Almería, Almería, Spain.

16

17 6 Andalusian Centre for the Monitoring and Assessment of Global Change  
18 (CAESCG), University of Almería, Almería, Spain.

19

20 7 Sobrarbe-Pirineos UNESCO Global Geopark. Boltaña. Spain.

21 8 Godwin Laboratory for Palaeoclimate Research, Department of Earth Sciences,  
22 University of Cambridge, Cambridge, UK

23

24 \*Correspondence: Miguel Bartolomé (mbart@ipe.csic.es)

25

26 **Abstract (250 words)**

27 Ice caves are one of the least studied parts of the cryosphere, particularly those  
28 located in inaccessible permafrost areas at high altitudes or high latitudes. We  
29 characterize the climate dynamics and the geomorphological features of Devaux  
30 cave, an outstanding ice cave in the Central Pyrenees on the French-Spanish  
31 border. Two distinct cave sectors were identified based on air temperature and



32 geomorphological observations. The first one comprises well-ventilated galleries  
33 with large temperature oscillations likely influenced by a cave river. The second  
34 sector corresponds to more isolated chambers, where air and rock temperatures  
35 stay below 0°C throughout the year. Seasonal layered ice and hoarfrost occupy  
36 the first sector, while transparent, massive perennial ice is present in the isolated  
37 chambers. Cryogenic calcite and gypsum are mainly present within the perennial  
38 ice. During winter, the cave river freezes at the outlet, resulting in a damming and  
39 back-flooding of the cave. We suggest that relict ice formations record past  
40 damming events with subsequent congelation.  $\delta^{34}\text{S}$  values of gypsum indicate  
41 that the sulfate originated from the oxidation of pyrite present in the bedrock.  
42 Several features including the air and rock temperatures, the absence of drips,  
43 the low loss of ice, and the location of ice bodies in the cave indicate the cave  
44 permafrost is the result of a combination of undercooling by ventilation and  
45 diffusive heat transfer from the surrounding permafrost, reaching ~200 m below  
46 the surface.

47 **Keywords:** Ice cave, cave monitoring, cryogenic cave carbonates, cryogenic  
48 gypsum, Devaux cave.

## 49 1. Introduction

50 Mountain areas are one of the most susceptible environments to current climate  
51 change (Hock et al., 2019). In the mid-latitudes, high-altitude areas are subject to  
52 mountain permafrost, a very sensitive and unstable phenomenon that responds  
53 quickly to environmental changes (Harris et al., 2003; Biskaborn et al., 2019) due  
54 to the number of factors. They influence the spatial distribution of mountain  
55 permafrost, including snow cover distribution and thickness, topography, water  
56 availability, surface temperature and rock temperature (Gruber and Haeberli,  
57 2009). Due to this number of processes multidisciplinary studies including,  
58 among others, rock temperature measurements in boreholes, the bottom  
59 temperature of snow cover (BTS), a variety of geophysical techniques, and  
60 thematic maps (geomorphology, thermal) are needed to gain a comprehensive  
61 understanding (e.g. Lewkowicz and Ednie, 2004; Serrano et al., 2019; Biskaborn  
62 et al., 2019). On the other hand, the study of paleo-permafrost (e.g. Vaks et al.,  
63 2020), modern permafrost, specifically mountain permafrost (e.g., Supper et al.,



64 [2014; Scandroglio et al., 2021](#)), sheds light on past, present and future  
65 developments of permafrost areas, an issue of vital importance in the context of  
66 global warming. Studies of past permafrost require sedimentary records, which  
67 are locally preserved in caves located at high altitudes and/or high latitudes.

68 Ice caves are defined as cavities in rock hosting perennial ice that results from  
69 the transformation of snow and/or the freezing of infiltrating water reaching the  
70 cave ([Perşoiu and Lauritzen, 2018](#)). Cave ice can be dated and used as a  
71 valuable paleoclimate archive in non-polar areas (e.g., [Stoffel et al., 2009; Spötl  
72 et al., 2013; Perşoiu et al., 2017; Kern et al., 2018; Sancho et al., 2018a; Leunda  
73 et al., 2019; Munroe, 2021; Racine et al., 2022](#)). Furthermore, temporal and  
74 spatial changes in past permafrost distribution have been identified using  
75 speleothems (stalagmites, flowstones) in circumpolar and polar regions (e.g.,  
76 [Vaks et al., 2013, 2020; Moseley et al., 2021](#)) as well as in mid-latitude regions  
77 (e.g., [Lundberg and McFarlane, 2007; Fankhauser et al., 2016; Lechleitner et al.,  
78 2020](#)). Recently, coarse cryogenic cave carbonates ( $CCC_{\text{coarse}}$ ), that form during  
79 slow freezing of water inside caves, have been used as indicator of permafrost  
80 degradation, permafrost thickness, and subsurface ice formation ([Žák et al.,  
81 2004, 2012; Richter et al., 2010; Luetscher et al., 2013; Orvošová et al., 2014;  
82 Spötl and Cheng, 2014; Bartolomé et al., 2015; Dublyansky et al., 2018; Koltai  
83 et al., 2020; Munroe et al., 2021](#)).

84 Many ice caves are located in areas where the mean annual air temperature  
85 (MAAT) outside the cave is above  $0^{\circ}\text{C}$  ([Perşoiu and Lauritzen, 2018](#)) and,  
86 therefore, are highly susceptible to future climate warming ([Kern and Perşoiu,  
87 2013](#)). These ice caves are local thermal anomalies which are controlled by the  
88 cave geometry and the associated ventilation pattern. Their ice deposits  
89 represent sporadic permafrost occurrences and do not inform about the wider  
90 thermal environment. In contrast, at high altitudes and high latitudes ice deposits  
91 are still preserved under the current climate change. There, mountain permafrost  
92 is limited to areas where a periglacial belt is present, with  $MAAT \leq 0^{\circ}\text{C}$ . For  
93 example, in the European Alps, discontinuous mountain permafrost is observed  
94 between 2600 and 3000 m a.s.l. ([Boeckli et al., 2012](#)), while in southern Europe  
95 permafrost is generally absent (i.e. not observed even on the highest massif of  
96 the Iberian Peninsula, [Gómez-Ortiz et al., 2019](#)). In the Central Pyrenees few



97 studies suggest the possible presence of permafrost above 2750 m a.s.l.  
98 ([Serrano et al., 2019, 2020](#); [Rico et al., 2021](#)), and the presence of a few ice  
99 caves has only been documented (e.g. [Sancho et al., 2018a](#); [Serrano et al.,](#)  
100 [2018](#)).

101 The aim of this study is to characterize the permafrost conditions in Devaux cave,  
102 a high-altitude ice cave in the Central Pyrenees. We monitored air, water and  
103 rock temperatures and used cryogenic cave deposits to i) document the  
104 distribution of permafrost within this cave, and ii) study the processes that  
105 resulted in perennial cave ice bodies and associated cryogenic mineral  
106 occurrences.

107

## 108 **2. Study site**

109 Devaux cave opens at ~2838 m a.s.l. in the NE cliff of Gavarnie cirque (France)  
110 of the Monte Perdido massif (MPm) in the Central Pyrenees (Fig. 1a). The cave  
111 is located between the Parc National des Pyrénées (France) and the Parque  
112 Nacional de Ordesa y Monte Perdido (Spain). Named after Joseph Devaux who  
113 discovered and explored it in 1928, the cave was later investigated with respect  
114 to its hydrogeology and microclimatology and preliminary descriptions of its  
115 deposits were reported (e.g., [Devaux, 1929](#); [Rösch and Rösch, 1935](#); [Rösch,](#)  
116 [1949](#); [Du Cailar and Dubois, 1953](#); [Requirand, 2014](#)).

117

118 The area is dominated by limestones and dolostones ranging from the Upper  
119 Cretaceous to the Eocene-Paleocene. MPm is the highest limestone karst area  
120 in Europe reaching up to 3355 m a.s.l. (Monte Perdido peak) (Fig. 1b). The  
121 nearest peaks to Devaux cave are Marboré (3248 m a.s.l.) and the three Cascada  
122 peaks (3164 m, 3111 m, and 3098 m a.s.l.). The limestone thickness above the  
123 cave varies between ~200 and 250 m (Fig. 2a). In Devaux, the galleries follow  
124 the axis of a NW-SE striking syncline (Fig. 1b). A river runs along the cave (Fig.  
125 2a, b). The cave has two known entrances: the lower one corresponds to the  
126 main outlet of the cave river (Brulle spring, North 1, ~2821 m a.s.l.), while the  
127 upper entrance is known as the “Porche” (South, ~2836 m a.s.l.) (Figs. 1c and  
128 2b). Between these two entrances, a small gallery (Spring North 2) opens +1.2 m



129 above Brulle spring (Fig. 1c). Brulle is one of the main springs in the Gavarnie  
130 cirque. This spring drains a catchment of  $\sim 2.6 \text{ km}^2$  (polje) located on the southern  
131 face of MPM between  $\sim 2850$  and  $3355 \text{ m a.s.l.}$  (Figs. 1b and, 1d). Major water  
132 flow is observed during late spring and early summer when snowmelt recharges  
133 a catchment characterised by shafts, sinkholes and small closed depressions  
134 (Fig. 1d). The water of Brulle spring feeds, together with some other springs  
135 located a few hundred meters below, the Gavarnie waterfall (Fig. 1b). A tracer  
136 experiment (du Cailar et al., 1953) indicated that part of the water of the Gavarnie  
137 waterfall, and thus likely also from Brulle spring, comes from a ponor in the Lago  
138 helado (lake, Fig. 1e), located  $\sim 2.3 \text{ km}$  to the east of Devaux cave (Figs. 1b and  
139 2a). The Gavarnie waterfall (Fig. 1b) turned green within  $\sim 21$  hours after injection  
140 but the water at Brulle spring was not directly checked (du Cailar et al., 1953).  
141 During the colder months, the spring water as well as the Gavarnie waterfall  
142 freeze.

143 The geomorphology of the area is dominated by karst, glacial and periglacial  
144 landforms. The area was strongly glaciated during the last glacial period on both  
145 sides of the massif (e.g. Reille and Andrieu, 1995; Sancho et al., 2018b;  
146 Bartolomé et al., 2021). Today, only two glacier relicts covered by scree deposits  
147 are present in the Gavarnie cirque (Fig. 1b): 1) the Cascada dead-ice which is  
148 located several hundred meters below Devaux cave, and 2) a dead-ice  
149 accumulation in the NE wall of the cirque. Till present close to Brulle spring, on  
150 the access to Devaux and in the Cascada glacier, point to a much larger glacier  
151 extent in the past, maybe corresponding to the Little Ice Age or even the  
152 Neoglacial advance recognized in the nearby Tucarroya (Fig. 1b) and Troumouse  
153 cirques (Gellatly et al., 1992; González Trueba et al., 2008; García-Ruiz et al.,  
154 2014, 2020).

155 The study area lies at the transition between Atlantic and Mediterranean climate,  
156 with generally cold and dry winters and warm and dry summers. In MPM, the  
157 annual zero isotherm is located at  $\sim 2900 \text{ m a.s.l.}$  (López-Moreno et al., 2016;  
158 Serrano et al., 2019). The wet seasons are fall and spring. The annual  
159 precipitation at the Góriz meteorological station ( $2150 \text{ m a.s.l.}$  and  $3 \text{ km SE}$  of the  
160 cave) averages  $1650 \text{ mm}$ . However, mass balance calculations of the nearby  
161 Monte Perdido glacier suggest that annual precipitation next to the cave may



162 exceed 2500 mm, as the snow depth measured in early May exceeds on average  
163 3 m (López-Moreno *et al.*, 2019). In the MPm, discontinuous permafrost is  
164 present between ~2750 and ~2900 m a.s.l. and becomes more frequent above  
165 ~2900 m a.s.l. on the northern side (Serrano *et al.*, 2019). Periglacial activity is  
166 characterized by rock glaciers, solifluction lobes and patterned ground (Feuillet,  
167 2011).

168

### 169 **3. Material and methods**

#### 170 **3.1 Cave survey and mapping**

171 A survey of Devaux cave was conducted using a compass and clinometer as well  
172 as a laser distometer (Disto-X, Heeb, 2014). In addition to cave ice, chemical and  
173 clastic deposits were mapped inside the cave. These features were overlain onto  
174 the cave survey to produce a geomorphological cave map (Fig. 2b). The labelling  
175 of the cave chambers (A to K) follows the nomenclature introduced by Devaux  
176 (1929) and Rösch and Rösch (1935).

177 A map of potential solar radiation (RAD) of the MPm was obtained using an  
178 algorithm which considers the effects of the surrounding topography on  
179 shadowing considering the position of the sun. RAD was calculated for every  
180 month of the year and then averaged to obtain an annual mean. Details of this  
181 computation can be found in Pons and Ninyerola (2008).

#### 182 **3.2 Cave monitoring**

183 The cave consists of large rooms (e.g., room F, or those located beyond SCAL  
184 chatière) connected by small galleries (Fig. 2b), locally with narrow passages  
185 (e.g., galleries close to SPD room or SCAL chatière, Fig. 2b). 15 stations were  
186 installed in the outmost ~350 m of the cave to monitor air (11 sensors), water (2  
187 sensors) and rock temperature (2 sensors) (Fig. 2b). Cave air temperature  
188 variations were recorded using different devices (Hobo Pro v2 U23-001 (accuracy  
189  $\pm 0.25^{\circ}\text{C}$ , resolution  $0.02^{\circ}\text{C}$ ), Tinytag Talk 2 (accuracy  $\pm 0.5^{\circ}\text{C}$ , resolution,  $0.04^{\circ}\text{C}$ )  
190 and ELUSB2 (accuracy  $\pm 0.21^{\circ}\text{C}$ , resolution  $0.5^{\circ}\text{C}$ )). The cave river temperature  
191 was recorded at two points; the first site (W7) was located close to the Brulle  
192 spring (Fig. 2b; Hobo TiDBit V2, accuracy  $\pm 0.21^{\circ}\text{C}$ , resolution  $0.02^{\circ}\text{C}$ ) and, the



193 second site (W6) was located in room F (Fig.2b; Hobo UA-001-08; accuracy  
194  $\pm 0.53^{\circ}\text{C}$ , resolution  $0.4^{\circ}\text{C}$ ). Both sensors were installed at a depth of 20 cm.  
195 Finally, rock temperature was recorded at two sites (R1 and R2 in room D and K,  
196 respectively) using a Hobo U23-003 device (accuracy  $\pm 0.25^{\circ}\text{C}$ , resolution  
197  $0.02^{\circ}\text{C}$ ). Each sensor has two external temperature probes (channels 1 and 2,  
198 Ch1-Ch2). These temperature probes were installed in two drill holes of 60 cm  
199 depth,  $\sim 1.5$  to 2 m from each other.

200 We monitored the cave during different time intervals between 2011 and 2015,  
201 while a continuous monitoring was carried out between July 2017 and July 2021.  
202 We calculated the maximum, minimum and mean temperatures as well as the  
203 number of frost/warm days for each sensor and site (Fig. 2b). Changes in the ice  
204 morphology were evaluated using wall marks measured at four points since 2013  
205 in room G and using one point during 2020-2021 in room SPD (Fig. 2b) using a  
206 digital sliding caliper.

207 The outside temperature was measured at two points in the MPm, at the “Porche”  
208 entrance ( $\sim 2836$  m a.s.l.) and on the southern face of MPM at  $\sim 2690$  m a.s.l. For  
209 comparison, these temperature records were corrected assuming an adiabatic  
210 lapse rate of  $0.55^{\circ}\text{C } 100^{-1}$  m (López-Moreno et al., 2016; Navarro-Serrano et al.,  
211 2018) to an elevation of  $\sim 2850$  m a.s.l., corresponding approximately to the lower  
212 limit of the hydrological catchment area of Devaux. In both cases, the temperature  
213 was measured using Tinytag Talk 2 sensors with a radiation shield. These data  
214 were compared to the temperature record from the Pic du midi de Bigorre  
215 meteorological station (PMBS; 2011-2020) (2860 m a.s.l.,  $\sim 28$  km N of Devaux)  
216 obtained from Météo-France. Moreover, the homogenised MAAT dataset since  
217 1882 from PMBS (Bücher and Dessens, 1991; Dessens and Bücher, 1995) was  
218 used to identify long-term climatic trends.

### 219 **3.3 Mineralogy, water and mineral sampling**

220 X-ray diffraction (XRD) analyses were performed on sulfate and carbonate  
221 crystals from rooms G, D and K, as well as on sulphide and oxidized crystals  
222 thereof from the host rock. The analyses were performed at the Geosciences  
223 Institute in Barcelona (GEO3-BCN-CSIC) using a Bruker-AXS D5005 powder  
224 diffractometer configured in theta-2 theta geometry.



225 Samples of cave drips, ice and river water were analysed for major ions by ion  
226 chromatography (IC) at the laboratories of the Pyrenean Institute of Ecology  
227 (Zaragoza). Carbonate alkalinity was determined by titration within 24 hours after  
228 sampling.

229 Sixteen samples, including sulfate crystals, dissolved sulfate and pyrite crystals  
230 were selected for sulfur isotope analyses at the Godwin Laboratory for  
231 Paleoclimate Research of the University of Cambridge (UK). For gypsum  
232 samples, ~5 mg of powdered gypsum were dissolved in deionized water at 45°C  
233 overnight. Then, a BaCl<sub>2</sub> solution (50 g/L) was added to induce BaSO<sub>4</sub>  
234 precipitation. In the case of water samples, BaCl<sub>2</sub> was added directly to the  
235 sample. Subsequently, 6M HCl was added to remove carbonates and the BaSO<sub>4</sub>  
236 precipitate was rinsed several times with deionized water. Finally, BaSO<sub>4</sub> was  
237 dried at 45°C overnight. Sulfates dissolved in water were precipitated using the  
238 same method.

239 Isotope measurements were carried out using a Flash Elemental Analyzer (Flash-  
240 EA) at 1030 °C. The samples were folded in tin capsules. After sample  
241 combustion, the generated SO<sub>2</sub> was measured by continuous-flow gas source  
242 isotope ratio mass spectrometry (Thermo Scientific, Delta V Plus). Samples were  
243 run in duplicate and calibration was accomplished using NBS-127. The  
244 reproducibility (1σ) of δ<sup>34</sup>S was better than 0.2‰, similar to the long-term  
245 reproducibility of the standard over the run (0.2‰). δ<sup>34</sup>S isotope values are  
246 reported relative to VCDT (Vienna-Canyon Diablo Troilite).

247

## 248 **4. Results**

### 249 **4.1 Devaux cave description**

250 Devaux cave is ~2500 m long and comprises three distinct levels (Fig. 2b). The  
251 lower and the middle levels correspond to the Brulle spring (0 m), and the  
252 “Porche” entrance (~+14.5 m), respectively. The third one comprises chambers  
253 and galleries +21 m to +29 m above the Brulle spring (Fig. 2b). In the inner part  
254 of the cave, some unexplored vertical chimneys may connect to sinkholes in the  
255 catchment above the cave (Fig. 2a). The main ice deposits are located in rooms  
256 D, G, SPD and K (Fig. 2b). Except for SPD, these chambers located above the



257 Porche entrance (between ~+1 and +7 m) can be accessed via ascending  
258 passages.

259 During the cold season, the cave river starts freezing at the spring and the ice  
260 then expands backward into room F (Fig. 2b). The ice totally or partially clogs the  
261 main gallery and dams the water inside the cave forming a small lake (cf. also  
262 [Rösch and Rösch, 1935](#)). This process is important for the seasonal ice extent  
263 as the flooding of the cave depends on whether the springs (North 1 and North  
264 2) are frozen or not (e.g., [Rösch and Rösch, 1935](#)). Webcam observations  
265 (Gavarnie, Oxygène hut) suggest a possible freezing of the Brulle spring from  
266 late November to mid-May simultaneous with the freezing of the Gavarnie  
267 waterfall. Moreover, historical photos (e.g., [Devaux, 1929](#); [Rösch and Rösch,](#)  
268 [1935](#)) and our own observations show that snow during winter and spring can  
269 reach the Brulle entrance - a situation that also favours the blocking of the  
270 springs. As a result of such flooding events, slackwater deposits are present in  
271 the cave entrance zone, but locally also further into the cave (e.g., in rooms I, J,  
272 K and SCAL chatière, along the main gallery; Fig. 2b) while silty sediments are  
273 found at elevated positions with respect to the river level (e.g., in rooms D and  
274 G). Sandy sediments dominate in the large rooms located beyond the SCAL  
275 chatière. Two such successions (~1 m thick) comprising hundreds of rhythmic  
276 fine sand-silt layers are present in elevated areas with respect to the current river,  
277 witnessing major events of back-flooding.

278 Observations made during summer show a dominant air-flow direction from the  
279 inner to the outer parts of the cave, exiting through the Brulle and Porche  
280 entrances. Conversely, the opposite is expected for the cold season (chimney  
281 effect). When the Brulle spring is partially clogged by the ice during early summer  
282 forcing the stream to flow below the ice, air flows from room F to C (Fig. 2b) (e.g.,  
283 summer 2021). The air flow is imperceptible in rooms D, G, and close to K located  
284 away from the main cave passages.

#### 285 **4.2 Climate setting of Devaux cave**

286 The MAAT at the elevation of Devaux cave is ~0 °C (-0.04 °C; 2017-2021). On  
287 the other hand, a positive MAAT (1.8 °C) is recorded on the southern side of the  
288 MPm at a similar altitude (Fig. 3a). Maximum and minimum air temperatures



289 outside the cave vary between 24.5 °C and -17.2 °C (hourly values, 2017-2021).  
290 The PMBS MAAT record (Fig. 3b) shows an increase of ~+1.5 °C since the  
291 beginning of the measurements in 1882. Before 1985, temperatures below 0°C  
292 dominated the annual cycle, while positive MAATs became more frequent in  
293 recent years. Minimum temperatures also show an increase of ~+2.5 °C, while  
294 the maximal annual temperatures do not show a clear trend. The north-facing  
295 Gavarnie cirque is associated with a clear RAD anomaly (Fig. 4). Values lower  
296 than 215 kWh/m<sup>2</sup> are observed at ~2000 m and between ~2800 and 2900 m,  
297 corresponding to the cirque bottom, the area located behind La Torre peak and  
298 the surroundings of Devaux cave. At the cave site the RAD value is only 390  
299 kh/m<sup>2</sup>, in stark contrast to the summit areas and surroundings where the RAD  
300 often exceeds 1500 kWh/m<sup>2</sup> (Fig. 4).

301 While the mean daily air temperature (MDAT) at the cave entrance (purple line in  
302 Fig. 5) and the temperature series from PMBS (pink line in Fig. 5) agree in their  
303 absolute values, the variability of MDAT at the Devaux entrance is lower than at  
304 the PMBS. This pattern could be related to local topographic conditions leading,  
305 for instance, to less RAD, or to the position of the sensor in the cliff (less night  
306 emissivity). Given this radiation contrast, warmer temperatures prevail on the  
307 southern side of the MPm (Fig. 4), favouring early snowmelt in spring and early  
308 summer, while at the same time the temperature stays below 0 °C in the cave's  
309 surroundings.

#### 310 **4.3 Devaux cave temperature variations**

311 The cave can be separated into distinct areas depending on their thermal regime:  
312 ventilated galleries (rooms A, B, C, F and the main gallery from SPD to K) and  
313 those off the main air flow path (rooms D, G - Figs. 2b, 5).

##### 314 **4.3.1 Well-ventilated cave parts**

315 Air temperature data show large seasonal oscillations at T<sub>2air</sub>, T<sub>5air</sub>, T<sub>10air</sub> T<sub>11air</sub>,  
316 T<sub>12air</sub>, W<sub>6water</sub>, W<sub>7water</sub> and R<sub>2rock</sub> sensors. All sensors except T<sub>11air</sub>, T<sub>12air</sub>, and  
317 R<sub>2rock</sub> show a few days with positive temperatures during summer. Sensor T<sub>2air</sub>  
318 (2011-2012, Fig.5a), which is also the closest to the Porche entrance, shows the  
319 highest correlation with the external temperature (0.73, p<0.001). Sensor T<sub>5air</sub>  
320 (2017-2021, Fig. 5d) in room B also shows a high correlation with the outside



321 temperature from November to May (0.82,  $p < 0.001$  (2017-2018); 0.66,  
322  $p < 0.001$  (2018-2019); 0.66,  $p < 0.001$  (2019-2020); 0.86,  $p < 0.001$  (2020-2021)),  
323 while during summer and fall correlations with external temperatures are slightly  
324 weaker (0.52,  $p < 0.001$  (2017-2018); 0.37,  $p < 0.001$  (2019-2020); 0.66  
325  $p < 0.001$  (2020-2021)). Sensor T11<sub>air</sub> (2017-2021, Fig. 5d) is located in SPD room.  
326 Despite being a well-ventilated gallery, the sensor is relatively protected from the  
327 air flow by the room morphology and shows lower correlations (0.45,  
328  $p < 0.001$  (2018-2019); 0.34,  $p < 0.001$  (2019-2020); 0.79  $p < 0.001$  (2020-2021))  
329 compared to T5<sub>air</sub>. Sensor T10 (2014-2015, Fig. 5c) does not show any significant  
330 correlation with the external temperature. Sensors T12<sub>air</sub> and R2<sub>rock</sub> are located  
331 in room K, and similar to T11<sub>air</sub>, the chamber morphology shields them from the  
332 air flow. Rock temperature sensor R2<sub>rock</sub> shows a slightly variable temperature  
333 ranging between  $-0.19^{\circ}\text{C}$  and  $-0.28^{\circ}\text{C}$  (mean of  $-0.24$  and  $-0.23^{\circ}\text{C}$  for channel 1  
334 and 2, respectively). Sensor T12<sub>air</sub> shows a low correlation with the external  
335 temperature ( $r^2 = 0.35$ ,  $p < 0.001$  (2018-2021)), and the same is observed for T<sub>ext</sub> -  
336 R2<sub>rock</sub> ( $r^2 = 0.35$ ,  $p < 0.001$  (2019-2021)). Meanwhile the correlation between T12<sub>air</sub>  
337 and R2<sub>rock</sub> is high but not significant ( $r^2 = 0.93$ ,  $p > 0.005$  (2019-2021)).

338 The water sensors W6<sub>water</sub> and W7<sub>water</sub> (Figs. 5b, c) recorded temperature  
339 variations during the years 2012-2013 and 2014-2015, respectively. Both sensors  
340 record a continuous temperature decline from the end of November to mid-  
341 January until the water freezes. At W7<sub>water</sub>, the temperature ranges between  $-0.3$   
342 and  $-5.8^{\circ}\text{C}$  between the end of fall and the beginning of winter, while between  
343 January and the beginning of June, the temperature stays close to  $0^{\circ}\text{C}$ . At W6  
344<sub>water</sub>, the temperature reached a minimum of  $-1.7^{\circ}\text{C}$  and shows smaller variations  
345 than at W7<sub>water</sub>. No significant correlation was found between the external  
346 temperature and the river water. Only W6<sub>water</sub> shows a small correlation with the  
347 external temperature when ice is absent (0.39  $p < 0.001$  and 0.40  $p < 0.001$ ).

348 For each monitored interval, the mean annual cave temperature at the T2<sub>air</sub>, T5<sub>air</sub>  
349 and T11<sub>air</sub> sensors is lower than the outside mean temperature for the same  
350 period ( $0.4^{\circ}$ ,  $2.0^{\circ}$ ,  $3.3^{\circ}\text{C}$  lower, respectively). The W6<sub>water</sub>, W7<sub>water</sub> and T10<sub>air</sub>  
351 sensors show mean temperatures higher than the external mean temperatures  
352 ( $1.6^{\circ}$ ,  $2.6^{\circ}$ ,  $2.5^{\circ}\text{C}$  higher, respectively). The periods 2011-2012 and 2017-2018



353 (at  $T_{2\text{air}}$  and  $T_{5\text{air}}$ , respectively) represent the coldest cave years of the monitoring  
354 period.

355

#### 356 **4.3.2 Poorly ventilated cave parts**

357 Air temperature sensors located in rooms D ( $T_{3\text{air}}$ ,  $T_{4\text{air}}$ ,  $T_{8\text{air}}$ ,  $R_{1\text{rock}}$ ) and G ( $T_{9\text{air}}$ )  
358 show a weak and/or insignificant correlation with the external temperature. All  
359 sensors show temperatures below 0 °C during the monitoring period with small  
360 oscillations. Sensor  $R_{1\text{rock}}$  (Fig. 5) recorded rock temperatures consistently below  
361 0°C during the entire monitoring period. This sensor shows constant rock  
362 temperatures (-1.24 °C and -1.27 °C for channels 1 and 2, respectively), similar  
363 within error to the cave air temperature ( $T_{3\text{air}}$ ,  $T_{9\text{air}}$ ; 2019-2021). All sensors  
364 except for  $T_{3\text{air}}$  (2011-2012, Fig. 5a) show mean air and rock temperatures lower  
365 than the mean external temperature during the same period (0.59 °C to 2.47°C  
366 lower). The muted temperature variations in these chambers reflect reduced heat  
367 exchange compared to the well-ventilated parts of the cave.

368

#### 369 **4.4 Cave deposits**

##### 370 **4.4.1 Ice**

371 Congelation ice formed by freezing of water within the cave is the most abundant  
372 type of ice, and four main ice deposits are located in chambers D, G, SPD, and  
373 K (Fig. 2b). The most relevant feature of these ice bodies is their transparency  
374 and massive aspect, i.e. the lack of layering (Figs. 6a, b). Transparent ice is  
375 present on the ceiling, blocking chimneys, galleries and fractures. The local loss  
376 of transparency is related to the presence of cryogenic cave minerals and/or air  
377 inclusions (Figs. 6a, b, c, d).

378 A highly transparent ice deposit covers the southwest wall of room D and blocks  
379 the access to a gallery (Fig. 6a). The height of this deposit reaches ~6 m, and its  
380 base is located ~20 m above the Brulle spring. The thickness of this ice deposit  
381 ranges from 4.5 to 14.5 m (horizontal laser measurements across the ice in the  
382 gallery blocked by ice) and the estimated volume ranges from ~350 to ~710 m<sup>3</sup>.



383 Three unconformities marked by cryogenic minerals were identified in this ice  
384 body.

385 In room G, an ice body (~25.8 to 29.6 m above the Brulle spring) is present on  
386 the ceiling (Fig. 6b) and the estimated ice volume is ~180 m<sup>3</sup>. A comparison with  
387 a historical photograph before 1953 (Casteret, 1953) suggests that the ice body  
388 has not changed significantly during the last ~69 years (Figs. 7a, b). Ice-rock  
389 distances measured at four points, however, reveal small changes at three of  
390 them. The first has retreated 9.8 mm since 2014 (mean 0.9 mm a<sup>-1</sup>, n=2), the  
391 second has retreated 19.2 mm since 2014 (mean 0.6 mm a<sup>-1</sup>, n=5), and the third  
392 one has retreated 15.8 mm since 2013 (mean 2.2 mm a<sup>-1</sup>, n=7). At ~80 m from  
393 the entrance, a small descending room (SPD) (Figs. 2b, 6c) hosts a small volume  
394 of ice. Measurements between 2020 and 2021 indicate a retreat of 20 mm a<sup>-1</sup>  
395 (n=1). A last major ice deposit is present ~280 m from the entrance (room K),  
396 where transparent and massive ice (~15.5 m above the Brulle spring) is filling a  
397 cupula or chimney (Figs. 2b, 6d). Additional ice bodies are present behind the  
398 SCAL chatière in the upper gallery (Fig. 2b), but they have not been studied.

399 In contrast to these massive ice deposits, layered ice of seasonal origin is present  
400 in small chambers adjacent to the river (E and F rooms) (Fig. 6e). This ice forms  
401 sheets of around 10-15 cm in thickness which are present in room F and nearby  
402 areas (Fig. 6f). This ice is related to the damming and freezing of water inside the  
403 cave when the Brulle spring freezes. Our visits from 2017 to 2021 revealed that  
404 most of the damming and subsequent ice formation in room F took place during  
405 winter and spring 2017-2018 corresponding with the coldest months (both inside  
406 the cave and outside) of the monitoring period (Fig. 5d). These ice slabs are  
407 characterized by flat surfaces on both sides and obviously record incomplete  
408 freezing of the dammed water. The ice sheets largely disappeared during  
409 summer and fall, and only strongly degraded ice remained in elevated areas of  
410 room F.

411 On the other hand, the ice sheets associated with earlier episodes of river  
412 damming and freezing have disappeared, and only linear colour changes remain  
413 as witnesses of such events on the walls of the room E (Fig. 8d). A historical  
414 photograph exemplifies these ice levels in the access between room F and E



415 (Fig. 8a). In August 1984 the ice was close to the ceiling and nearly 1 m thick  
416 (Fig. 8a; Marc Galy, pers. comm.). This contrasts with the low ice level in recent  
417 years (Fig. 8b). In total, three ice-level marks were identified in relation to back-  
418 flooding and subsequent freezing of ponded water (Figs. 8c, d). They appear at  
419 a lower elevation than the Porche entrance (c.+9.5, +9.2, +8.8, m with respect to  
420 the Brulle spring).

421 Another important feature is the presence of hoarfrost, which is observed in room  
422 B and along the gallery between SPD and K (Figs. 2b, 7g, 7h). The crystal size  
423 varies from few mm to 4 cm and appears to be upholstering some galleries and  
424 cupolas, forming aggregates that hang from the ceiling (Fig. 6h). Finally, seasonal  
425 ice formations (e.g., icicles and ice stalagmites), as well as drips are restricted to  
426 the outmost ~15 m, in the vicinity of both entrances, and in the innermost part of  
427 the cave (~ 500 m from the entrance). Seasonal ice formations are absent in cave  
428 sectors where transparent ice bodies and hoarfrost are present. Firn deposits  
429 derived from snow are restricted to the Porche entrance.

430

#### 431 **4.4.2 Mineral deposits**

432 They comprise mainly cryogenic cave minerals. XRD analyses of samples from  
433 rooms D, G and K yielded gypsum and calcite, while the sulfide crystals and their  
434 oxidation product present in the host rock were identified as pyrite and goethite,  
435 respectively. The presence of cryogenic gypsum in Devaux was already reported  
436 by [du Cailar and Dubois \(1953\)](#). In room D, gypsum was observed within the ice  
437 and on boulders (Figs. 9a, b, c). A total of three gypsum levels (lower, middle and  
438 upper, located at ~21.4, ~22.6 and ~23.9 m, respectively, with respect to the  
439 Brulle spring) were identified in the ice (Fig. 9a). Due to the progressive retreat of  
440 the ice body, some of these crystals are now present on the ice surface. Gypsum  
441 levels comprise large single crystals (0.5-1 cm in diameter), aggregates forming  
442 rafts (10 cm) up to 1 cm in thickness (Fig. 9b), as well as a fine crystalline fraction.  
443 Visual examination of the fine fraction under a binocular stereo microscope  
444 indicates the presence of small aggregates of cryogenic cave carbonates and  
445 gypsum (CCG) (<1 mm) including globular, single and twin morphologies (Fig.  
446 9d).



447

448 In room G, gypsum and carbonates crystals are present in the lower part of the  
449 ice deposit (Fig. 10e) and on blocks. There, CCC are larger (>10 mm) than in  
450 room D and include globular shapes and raft-like aggregates, similar to those  
451 reported by Žák et al. (2012). Some of these CCC show gypsum overgrowths  
452 (Fig. 9f). Across the ice surface, patches of globular CCC (sub-millilitre size) have  
453 been released by ice sublimation (Fig. 7a, b). In room SPD CCC and CCG ( $\leq 2$   
454 mm) are present within and on the ice (Figs. 2b, 7c). Finally, in room K, only few  
455 CCC were still present within the ice, while most of them form heaps of loose  
456 crystals covering blocks. Some of these CCCs exceed 5 mm in diameter. Crystal  
457 morphologies include rosettes, skeletons and rhombohedrons similar to those  
458 reported by Žák et al. (2012) as well as white tapered crystal aggregates. Beyond  
459 room K, regular carbonate speleothems (i.e. stalagmites, stalactites and  
460 flowstones) are present.

#### 461 **4.5 Cave water chemistry and sulfate isotopic composition**

462 The chemical composition of water in Devaux (n=22) cave is dominated by  
463 calcium and bicarbonate with relatively high Mg concentrations and locally also  
464 elevated sulfate concentrations (Table 1). Total dissolved solids (TDS, n=7) vary  
465 from 57 to 315 mg l<sup>-1</sup>. Devaux's dripwater has higher mean sulfate concentrations  
466 (65 mg l<sup>-1</sup>) than the cave river (11 mg l<sup>-1</sup>) and massive and seasonal ice (2.8-18  
467 mg l<sup>-1</sup>). Concerning the sulfur isotopic composition (Table 2), the  $\delta^{34}\text{S}$  value of  
468 dissolved sulfate in the dripwater is -14.4‰ (n=1), which is significantly higher  
469 than in cave river water (-28.5‰ to -27.3‰, n=2). Gypsum crystals in room D  
470 show homogeneous  $\delta^{34}\text{S}$  values ranging from -15.1‰ to -15.8‰ (n=7), while in  
471 room G the range from -12.3‰ to -11.9‰ (n=5). A pyrite sample from the host  
472 rock yielded a  $\delta^{34}\text{S}$  value of -12.7‰ (n=1).

### 473 **5. Discussion**

#### 474 **5.1. Processes controlling the thermal regime in Devaux cave and current** 475 **permafrost extent**

476 A complex spatial distribution and a high degree of heterogeneity are among the  
477 main characteristics of mountain permafrost (Gruber and Haeblerli, 2009). In  
478 Devaux cave the existence of permafrost can be related to a combination of two



479 processes: i) cave atmospheric dynamics, and ii) conductive heat transfer  
480 through the rock.

481 Devaux cave is characterized by mean air and rock temperatures lower than the  
482 external mean annual temperature (Fig. 5). The low cave temperatures in winter  
483 lead to an inward airflow and an associated negative thermal anomaly behind the  
484 cave entrance zone. Similar seasonal ventilation patterns have been observed in  
485 ice caves elsewhere (e.g., [Luetscher et al., 2008](#); [Colucci and Guglielmin, 2019](#);  
486 [Perçoiu et al., 2021](#)).

487 On the other hand, positive temperatures are observed both in the cave river and  
488 in the air at the cave entrance (Fig. 5), reflecting heat advected by water (river)  
489 and the influence of the external temperature (cf. [Luetscher et al., 2008](#); [Badino,](#)  
490 [2010](#)). The lack of correlation between the external and internal temperatures  
491 and the small temperature variability in rooms D, G, and K reflect their thermal  
492 isolation from well-ventilated cave parts. There, the apparent thermal equilibrium  
493 between the rock and the cave atmosphere ( $T_{\text{rock}}=T_{\text{air}}$ ) supports the notion that  
494 heat exchange is dominated by conduction through the bedrock.

495 The MAAT at the altitude of the cave is  $-0.04$  °C (2017-2021) suggesting that the  
496  $0$  °C isotherm is located close to the cave. Using an array of techniques (geomatic  
497 surveys, temperature monitoring, temperature at the base of the snowpack (BTS)  
498 and geomorphological and thermal mapping), [Serrano et al. \(2019\)](#) found mean  
499 annual ground temperatures between  $-1$  and  $-2$  °C on the northern slope of the  
500 MPm suggesting that discontinuous permafrost is present between 2750-2900 m  
501 a.s.l., with more continuous permafrost starts at 2900 m a.s.l. The orientation of  
502 the Gavarnie cirque, as well as the high slope angle, and shadow from the  
503 surrounding peaks favour the preservation of permafrost at lower elevations (e.g.,  
504 [Gubler et al., 2011](#)).

505

506 Given the high thermal inertia of the rock, the permafrost temperature at depth is  
507 still under the influence of past climate conditions (e.g., [Haeberli et al., 1984](#);  
508 [Noetzli and Gruber, 2009](#)) and, therefore, part of the current permafrost in the  
509 area could be inherited from previous colder times (e.g., [Colucci and Guglielmin,](#)  
510 [2019](#)). In particular, the low mean annual temperatures recorded at PMBS at the



511 beginning of the Industrial Era are favourable conditions for permafrost  
512 development in the recent past. We surmise that the current permafrost could be  
513 inherited from colder periods of the Little Ice Age.

514 In well-ventilated ice caves hoarfrost is the most dynamic ice formation on  
515 seasonal time scales. The presence of perennial hoarfrost is, however, indicative  
516 of a continuously frozen bedrock and thus representative of caves within the  
517 permafrost zone (e.g. [Luetscher and Jeannin, 2018](#); [Yonge et al., 2018](#)). In  
518 Devaux cave, perennial hoarfrost is observed in rooms where the bedrock is  
519 surrounded by small ice bodies (e.g., gallery close to SPD room, Fig. 6g). On the  
520 other hand, seasonal hoarfrost is present in ventilated galleries (A, B, C, F and  
521 between SPD and J). Seasonal hoarfrost in room B and C disappears at the end  
522 of summer, probably because of the heat delivered by the cave river, as recorded  
523 by the T5 sensor (Fig. 5).

524 The presence of permafrost in Devaux's catchment is supported by the absence  
525 of drips and/or seepage in the investigated cave passages (e.g., [Luetscher and](#)  
526 [Jeannin, 2018](#); [Vaks et al., 2020](#)). Active drips and seasonal ice formations are  
527 limited to the first ~15 m of the cave as well as to the inner part (beyond room K).  
528 Mountain permafrost thus penetrates ~350 m longitudinally from the East cliff of  
529 the Gavarnie cirque to the southern side of the massif, following a west-east  
530 direction. On the other hand, given the elevation of the cave and the topographic  
531 relief above the cave, the current maximum permafrost thickness (without taking  
532 into account the active layer) on the southern side of the MPm is ~200 m.

533

## 534 **5.2. The origin of ice in Devaux cave**

535 The transparent and massive character of Devaux's cave ice suggests that this  
536 ice formed by slow freezing of water dammed by ice at the spring. This model is  
537 consistent with the climate in the Gavarnie cirque, cave geomorphological  
538 observations, cave air and water temperatures as well as historical reports. The  
539 cave water level can rise by several meters as indicated by slackwater deposits  
540 upstream of the Brulle spring.

541



542 The distribution and characteristics of ice bodies in Devaux cave indicate that the  
543 hydraulic head rose by at least ~ 15 - 29 m, which is the elevation of the ice bodies  
544 in rooms G, F and K. This situation requires that all springs (including Porche)  
545 are blocked for a sufficiently long time to allow for complete freezing of these cave  
546 lakes. The lack of important unconformities in this massive ice (e.g., detrital  
547 layers), which are usually related to seasonal ablation (e.g., [Luetscher et al.,](#)  
548 [2007](#); [Stoffel et al., 2009](#); [Spötl et al., 2013](#); [Sancho et al., 2018a](#)), suggests that  
549 the deposit in room G it is the result of a single flood event. On the contrary, the  
550 small unconformities recognized in the ice body in room D suggest that several  
551 cycles of damming and subsequent ice formation cannot be discarded in the  
552 formation of this ice deposit.

553

554 Our observations indicate that under the current climate (both in the cave and  
555 outside) only part of the water dammed in rooms F and E freezes during winter  
556 and spring. This strongly suggests that the ice bodies in Devaux cave must have  
557 been associated with colder and/or longer events of ponding and freezing than  
558 today, when the cave was effectively sealed from the outside for prolonged times.  
559 We hypothesize that the advance of a glacier on the steep slopes of Devaux's  
560 surroundings could have contributed to the blockage of the spring, leading to  
561 backflooding and the formation of large ice bodies in the cave. In the study area,  
562 such periods of glacier growth occurred during the Little Ice Age and/or the  
563 Neoglacial ([González Trueba et al., 2008](#); [García-Ruiz et al., 2014, 2020](#)).

564

565 The freezing of a flooded cave passage cannot be explained by the advection of  
566 cold air alone. It is thus surmised that heat transfer through the host rock is a  
567 more plausible mechanism for the complete freezing of the ponded water. The  
568 cave ice bodies, just as the presence of cryogenic minerals, therefore represents  
569 a record of a long cold period or of several such episodes. Although the cryogenic  
570 minerals and in particular CCC<sub>coarse</sub> are typically associated with permafrost  
571 thawing during warm spells ([Žák et al., 2004](#); [Richter et al., 2010](#); [Žák et al., 2012](#);  
572 [Luetscher et al., 2013](#)), permafrost conditions prevailed during ice formation in  
573 Devaux cave. Thus, the water that feeds Devaux's springs infiltrated during late  
574 spring and summer from ponors at Lago helado and/or surrounding poljes (which



575 may have acted as local taliks). However, the heat supplied by this water may  
576 have probably not been enough to thaw the frozen host rock. It is thus very likely  
577 that the hostrock temperature was much lower and/or the outlets remained closed  
578 longer than today to allow for the complete freezing of the ponded water.

579

### 580 **5.2.1 Ice volume changes**

581 The colour changes in the walls close to the river (room E), the historical  
582 photograph as well as speleological reports point to large changes (several  
583 meters) of the height of the seasonal ice in the flood-prone sector of the cave  
584 (Figs. 8a, b). This ice is influenced by the heat exchanged between the water and  
585 the cave.

586 In contrast, changes in the ice volume are almost negligible in rooms D and G  
587 where the temperature is more constant and below 0°C (Figs. 7a, b). The ice  
588 body in room G retreats only by ~0.6 to ~2.2 mm a<sup>-1</sup>. A similar value (3 mm a<sup>-1</sup>)  
589 was observed in Coulthard cave (Alberta, British Columbia, [Marshall and Brown, 1974](#)),  
590 a cave located within permafrost ([Yonge et al., 2018](#)). Changes in the ice  
591 body in this cave were related to slow sublimation due to convective air flow inside  
592 the cave ([Marshall and Brown, 1974](#)). On the other hand, the ice in SPD room  
593 shows higher ice retreat rates (~ 20 mm a<sup>-1</sup>). Similar sublimation rates have been  
594 reported in others ice caves in the Pamir Mountains and the northern part of the  
595 Russian Platform ([Mavlyudov, 2008](#); [Žák et al., 2018](#)). Overall, Devaux's cave ice  
596 deposits show a remarkable stability which contrasts to the rapid changes  
597 observed in ice caves outside permafrost areas ([Kern and Perşoiu, 2013](#); [Perşoiu  
598 et al., 2021](#); [Wind et al., 2022](#)), including other ice caves in the Pyrenees and  
599 Picos de Europa ([Belmonte-Ribas et al., 2014](#); [Gomez-Lende et al., 2014, 2016](#)).

600

### 601 **5.3. Cryogenic cave minerals**

602 In Devaux cave, CCC and CCG are still present within the ice (Figs. 6, a, b, c, d).  
603 Worldwide, only very few *in situ* observations of coarse-grained cryogenic cave  
604 minerals are known (e.g., [Bartolomé et al., 2015](#); [Colucci et al., 2017](#)). [du Cailar](#)



605 and Dubois (1953) reported the presence of gypsum crystals at ~50 cm depth  
606 within the ice in Devaux cave. The first evidence of *in situ* CCC<sub>coarse</sub> in cave ice  
607 was reported from Sarrios 6, an ice cave at 2780 m a.s.l. on the southern slope  
608 of the MPm (Bartolomé et al., 2015). Colucci et al. (2017) documented the  
609 presence of CCC<sub>coarse</sub> in a small ice cave in the Italian Alps. Recently, Munroe et  
610 al. (2021) found CCC<sub>coarse</sub> in ice of Wonderland cave (Utah, USA). Because of  
611 the abundance of cryogenic cave minerals, the size of individual crystals and  
612 aggregates thereof, and their varied mineralogy, Devaux cave provides an  
613 additional opportunity for studying the origin of such cryogenic cave minerals.

614

615 The CCGs in Devaux cave represent, to our knowledge, the first occurrence of  
616 its kind in a carbonate karst terrain. So far, CCGs have only been reported from  
617 gypsum karst areas in Russia and Ukraine (Korshunov and Shavrina, 1998; Žák  
618 et al., 2018 and references therein). In those areas, tiny gypsum crystals (gypsum  
619 powder) form during rapid freezing of water. When ice sublimates in winter, this  
620 gypsum powder is released and accumulates on the ice surface. Eventually, the  
621 powder dissolves on the ice surface during spring and summer due to the  
622 increase in cave air humidity, and later recrystallizes forming a wide variety of  
623 delicate morphologies. CCGs from Devaux cave show features that do not  
624 correspond to those previously published from gypsum karst caves. In particular,  
625 the Devaux cave CCGs i) appear together with CCC<sub>coarse</sub> crystals ( $\geq 5$  mm in some  
626 cases, in rooms D and G), ii) the (raft-like) gypsum crystals are large (Fig. 9b)  
627 and, in some cases, are still found within the ice (Fig. 9a) and surrounded by  
628 milky ice rich in air inclusions (Fig. 9a, e), and iii) boulders are locally overgrown  
629 by gypsum (Fig. 9c).

630

631 Coarse-grained cryogenic cave minerals form in a semi-closed system, when the  
632 water freezes inside the caves at low freezing rates (Žák et al., 2004). Once  
633 supersaturation is reached, CCM start to crystallize. The formation of gypsum  
634 crystals requires the presence of dissolved sulfate which may relate to i)  
635 sedimentary gypsum deposits intercalated within carbonates (e.g., Sancho et al.,  
636 2004), ii) the presence of hydrothermal water containing H<sub>2</sub>S in relation with  
637 hydrocarbons (e.g., Hill, 1987), or iii) the oxidation of sulfides (e.g., pyrite)  
638 disseminated in limestones (e.g., Bottrell, 1991). In the case of Devaux cave



639 marine evaporite rocks (e.g., of the Upper Triassic Keuper facies) and  
640 hydrocarbons are absent in the catchment of the cave. The most plausible  
641 explanation for the presence of dissolved sulfate in Devaux's water is the  
642 oxidation of pyrite present in the limestone (du Cailar and Dubois, 1953;  
643 [Requirand, 2014](#)).

644

645 Water in Devaux cave contains moderate concentrations of sulfate.  $\delta^{34}\text{S}$  values  
646 of gypsum (-11.9 to -15.8 ‰), pyrite (-12.7 ‰), and dissolved sulfate (-14.4 ‰ in  
647 dripwater and -28.5 to -27.3 ‰ in Brulle spring water) are within the range of  
648 biogenic pyrite and differ notably from values of marine evaporites (10-35 ‰)  
649 ([Seal, 2006](#)). Thus, the  $\delta^{34}\text{S}$  values together with the geological setting of the  
650 cave support the hypothesis that disseminated pyrite in the host limestone is the  
651 main source of dissolved sulfate and subsequently of CCG. Only the dissolved  
652 sulfate  $\delta^{34}\text{S}$  values of Brulle spring are considerably more negative (-28.5‰ and  
653 -27.3‰). This may be a consequence of microbially mediated redox processes  
654 in the karst that discriminate against  $^{34}\text{S}$  ([Zerkle et al., 2016](#); [Temovski et al.,](#)  
655 [2018](#)). Further studies on the microbiology of the cave may shed light on these  
656 mechanisms and how the local sulfur cycle may have changed in the past.

657

658 In gypsum caves, dissolved sulfate dominates over the bicarbonate, and the  
659 typical crystallization sequence during freezing of water with high TDS is gypsum  
660 → carbonate (commonly calcite) → celestine ([Žák et al., 2018](#)). In Devaux cave,  
661 however, bicarbonate dominates over sulfate, and our observations show that  
662 gypsum crystals partly nucleated on CCC<sub>coarse</sub>. Accordingly, the crystallization  
663 sequence at Devaux cave is calcite → gypsum, taking place in a semi-closed  
664 system at low freezing rates.

665

666 The second aspect that makes the CCG in Devaux cave unique is the size and  
667 well-developed crystal shapes (Fig. 9 b), which differ notably from the much  
668 smaller sizes of gypsum crystals (20-200  $\mu\text{m}$ ) and gypsum powders (1-30  $\mu\text{m}$ )  
669 found in gypsum caves in Russia and Ukraine ([Žák et al., 2018](#) and references  
670 therein). Another characteristic of CCC and CCG occurrences in Devaux cave is  
671 the presence of milky ice surrounding them (Fig. 9a, e) which seems to be related



672 to the freezing process during the formation cryogenic minerals in a subaqueous  
673 environment.

674

675 Finally, the presence of gypsum aggregates overgrowing some blocks (Fig. 9c)  
676 supports the hypothesis of subaqueous gypsum formation. On the other hand,  
677 gypsum was never observed growing from the ceiling or the walls, thus allowing  
678 to discard its formation from seepage water followed by precipitation due to  
679 evaporation in the cave (e.g., [Gázquez et al., 2017, 2020](#)). In essence, all  
680 observations indicate that gypsum precipitated in a semi-closed subaqueous  
681 environment and has been preserved from later dissolution by the exceptionally  
682 dry environment of this ice cave. Gypsum precipitating from freezing waters has  
683 been also documented in the Arctic and the Antarctica ([Losiak et al., 2016](#);  
684 [Wollenburg et al., 2018](#)) and has been proposed as mechanisms for gypsum  
685 formation on Mars ([Losiak et al., 2016](#)).

686

## 687 **6. Conclusions**

688 The investigation of Devaux ice cave, based on cave monitoring, geomorphology,  
689 and geochemical analyses, provides exceptional insights into the origin of  
690 mountain permafrost and associated processes and deposits.

691 - Devaux cave consists of two parts characterised by different thermal regimes:

692 1) the near-entrance parts and the main gallery showing large temperature  
693 fluctuations and cave air temperatures seasonally exceeding 0°C. These  
694 passages are influenced by an advective air flow and the heat released by the  
695 cave river. 2) The inner sector and isolated chambers are characterized by  
696 muted thermal oscillations and temperatures constantly below 0°C. There, the  
697 cave air temperature is mainly controlled by heat conduction through the  
698 bedrock.

699

700 - Devaux cave is impacted by backflooding in late winter/early spring when the  
701 main outlets freeze, damming the water inside the cave forming a lake. The  
702 blocking of the outlets requires temperatures below 0°C in the Gavarnie cirque,  
703 while on the southern side of the Monte Perdido massif, temperatures above  
704 0°C allow water infiltration.



705  
706 - The absence of dripwater in most parts of the cave together with the presence  
707 of perennial/seasonal hoarfrost, and the location of massive ice bodies on the  
708 ceiling and/or filling cupulas and galleries are indicative of frozen bedrock  
709 surrounding the cave. Permafrost at Devaux cave is attributed to a combination  
710 of rock undercooling by cave air ventilation and the local climate setting giving  
711 rise to the development and/or preservation of permafrost inherited from past  
712 colder periods. Currently, permafrost seems to be present above the cave  
713 reaching a maximum thickness of ~200 m and a lateral extension of ~350 m  
714 towards the southern face of the Monte Perdido massif.

715  
716 - We report the first deposits of cryogenic gypsum in a limestone-hosted ice cave.  
717 Most of the cryogenic minerals are still within the ice and surrounded by milky  
718 ice rich in air inclusion. Gypsum precipitation occurred subaqueously as a result  
719 of slow freezing, following CCC formation.  $\delta^{34}\text{S}$  values show that the sulfate  
720 originated from the oxidation of pyrite present in the limestone.

721  
722 - Current climate conditions seem to be still favourable for the preservation of ice  
723 within this cave. This situation contrasts to the large loss in other ice caves  
724 elsewhere. The ice deposits in Devaux allow unique insights into processes  
725 leading to the formation of cryogenic carbonates and sulfates, and represents  
726 an ideal site to better understand the mountain permafrost evolution in the  
727 Monte Perdido massif and the Pyrenees in general.

#### 728 **Competing interests**

729 No competing of interest

#### 730 **Authors contribution**

731 MB conceived the project, planned fieldwork and the sampling strategy. AM  
732 obtained funding for this work. MB and GC installed and maintained the sensors  
733 and performed the fieldwork. GC contributed with cave monitoring data from 2011  
734 to 2015. MB analysed monitoring, geomorphological, and geochemical data. FG  
735 performed  $\delta^{34}\text{S}$  analyses using the facilities provided by AVT. JILM created the  
736 radiation map. MB designed the figures and wrote a first draft of the manuscript.  
737 ML significantly contributed to the discussion of the data. ML and AM reviewed



738 all versions of the manuscript. All authors reviewed the manuscript and  
739 contributed to the results, discussion, and final interpretation. All authors  
740 approved its submission.

#### 741 **Acknowledgements**

742 We thank the directorates of the Parc National des Pyrénées (France) and the  
743 Ordesa y Monte Perdido National Park (Spain) for their permission to investigate  
744 Devaux cave. We want to especially thank Marc Galy for his cave survey which  
745 improves noticeably previously published surveys and for the historical photo of  
746 1984. Also, we thank Météo France for providing climate data from the Pic du  
747 midi de Bigorre station. We thank Maria Leunda for a critical review and  
748 suggestions to the first draft of the manuscript. We also thank Jerome Labat  
749 (SSPPO), Claude Novoa, Alvaro Palacios, Maria Leunda, José Leunda, David  
750 Serrano, the Góriz hut staff ([www.goriz.es](http://www.goriz.es)), and the Palazzo family  
751 ([www.hotelpalazio.com](http://www.hotelpalazio.com)) for their invaluable help during fieldwork. We thank Paul  
752 Cluzon for the photo of Fig. 1d, and Claude Requirand for his report about Devaux  
753 cave. The authors would like to acknowledge the use of the Servicio General de  
754 Apoyo a la Investigación-SAI, University of Zaragoza, and Alberto Barcos (IPE-  
755 CSIC) for the chemical water analyses. This study contributes to the work carried  
756 out by the DGA research group Procesos Geoambientales y Cambio Global (ref.:  
757 E02-20R) and the MERS research group 2017 SGR 1588.

#### 758 **Financial support**

759 This research has been supported by the following projects which were funded  
760 by the National Parks Autonomous Agency (OAPN) (OCHESTRA-ref  
761 2552/2020), the Spanish Agencia Estatal de Investigación (AEI-Spain)  
762 (PICACHU-ref PID2019-106050RB-I00), (SPYRIT- ref CGL2016-77479-R), the  
763 PaleolCE EXPLORA project (ref. CGL2015-72167-EXP) and the Comité régional  
764 de spéléologie de Nouvelle Aquitaine. Miguel Bartolomé was supported by a  
765 postdoctoral fellowship of the Juan de la Cierva-Formación program provided by  
766 the Spanish Ministry of Science (ref.: FJCI-2017-31725) and OCHESTRA-ref  
767 2552/2020. Fernando Gázquez was financially supported by a Ramón y Cajal  
768 Fellowship (RYC2020-029811-I) of the Spanish Government (Ministerio de  
769 Economía y Competividad).



770

## 771 References

- 772 Badino, G., 2010. Underground meteorology - "What's the weather underground?" *Acta*  
773 *Carsologica* 39, 427-448, <https://doi.org/10.3986/ac.v39i3.74>
- 774 Bartolomé, M., Sancho, C., Benito, G., Medialdea, A., Calle, M., Moreno, A., Leunda, M.,  
775 Luetscher, M., Muñoz, A., Bastida, J., Cheng, H., Edwards, R.L., 2021. Effects of  
776 glaciation on karst hydrology and sedimentology during the Last Glacial Cycle:  
777 The case of Granito cave, Central Pyrenees (Spain). *Catena* 206, 105252.  
778 <https://doi.org/10.1016/j.catena.2021.105252>
- 779 Bartolomé, M., Sancho, C., Osácar, M.C., Moreno, A., Leunda, M., Spötl, C., Luetscher,  
780 M., López-Martínez, J., Belmonte, A., 2015. Characteristics of cryogenic  
781 carbonates in a Pyrenean ice cave (northern Spain). *Geogaceta* 58 107–110.
- 782 Belmonte-Ribas, Á., Sancho, C., Moreno, A., Lopez-Martinez, J., Bartolome, M., 2014.  
783 Present-day environmental dynamics in ice cave A294, central Pyrenees, Spain.  
784 *Geogr. Fis. E Din. Quat.* 37, 131–140. <https://doi.org/10.4461/GFDQ.2014.37.12>
- 785 Biskaborn, B.K., Smith, S.L., Noetzli, J., Matthes, H., Vieira, G., Streletskiy, D.A.,  
786 Schoeneich, P., Romanovsky, V.E., Lewkowicz, A.G., Abramov, A., Allard, M.,  
787 Boike, J., Cable, W.L., Christiansen, H.H., Delaloye, R., Diekmann, B., Drozdov,  
788 D., Etzelmüller, B., Grosse, G., Guglielmin, M., Ingeman-Nielsen, T., Isaksen, K.,  
789 Ishikawa, M., Johansson, M., Johannsson, H., Joo, A., Kaverin, D., Kholodov, A.,  
790 Konstantinov, P., Kröger, T., Lambiel, C., Lanckman, J.-P., Luo, D., Malkova, G.,  
791 Meiklejohn, I., Moskalenko, N., Oliva, M., Phillips, M., Ramos, M., Sannel, A.B.K.,  
792 Sergeev, D., Seybold, C., Skryabin, P., Vasiliev, A., Wu, Q., Yoshikawa, K.,  
793 Zheleznyak, M., Lantuit, H., 2019. Permafrost is warming at a global scale. *Nat.*  
794 *Commun.* 10, 264. <https://doi.org/10.1038/s41467-018-08240-4>
- 795 Boeckli, L., Brenning, A., Gruber, S., Noetzli, J., 2012. A statistical approach to modelling  
796 permafrost distribution in the European Alps or similar mountain ranges. *The*  
797 *Cryosphere* 6, 125–140. <https://doi.org/10.5194/tc-6-125-2012>
- 798 Bottrell, S.H., 1991. Sulphur isotope evidence for the origin of cave evaporites in Ogof y  
799 Daren Cilau, south Wales. *Mineral. Mag.* 55, 209–210.  
800 <https://doi.org/10.1180/minmag.1991.055.379.09>
- 801 Bücher, A., Dessens, J., 1991. Secular trend of surface temperature at an elevated  
802 observatory in the Pyrenees. *J. Clim.* 4, 859–868. [https://doi.org/10.1175/1520-0442\(1991\)004<0859:STOSTA>2.0.CO;2](https://doi.org/10.1175/1520-0442(1991)004<0859:STOSTA>2.0.CO;2)
- 803 Casteret, N., 1953. Dans les glaces souterraines. Les plus élevées de Monde. Libraire  
804 Académique Perrin, Paris, p. 93.
- 805 Colucci, R., Luetscher, M., Forteet, E., Guglielmin, M., Lenaz, D., Princivalle, F., Vita, F.,  
806 2017. First alpine evidence of in situ coarse cryogenic cave carbonates  
807 (CCCcoarse). *Geogr. Fis. E Din. Quat.* 53–59.  
808 <https://doi.org/10.4461/GFDQ.2017.40.5>
- 809 Colucci, R.R., Guglielmin, M., 2019. Climate change and rapid ice melt: Suggestions  
810 from abrupt permafrost degradation and ice melting in an alpine ice cave. *Prog.*  
811 *Phys. Geogr. Earth Environ.* 0309133319846056.  
812 <https://doi.org/10.1177/0309133319846056>
- 813 Dessens, J., Bücher, A., 1995. Changes in minimum and maximum temperatures at the  
814 Pic du Midi in relation with humidity and cloudiness, 1882–1984. *Atmospheric*  
815 *Res., Minimax Workshop* 37, 147–162. [https://doi.org/10.1016/0169-8095\(94\)00075-O](https://doi.org/10.1016/0169-8095(94)00075-O)
- 816 Devaux, J., 1929. Nouvelle grotte Marboréenne. *La Natura* 102–107.
- 817 du Cailar, J., Couderc, J., Dubois, P., 1953. La source du Gave de Pau. *Annales de*  
818 *Spéléologie* 181–203.



- 821 du Cailar, J., Dubois, P., 1953. Sur quelques modalités de formation et d'évolution des  
822 dépôts cristallins dans les cavités de haute altitude. In: Premier Congrès  
823 International de Spéléologie. Paris, Tome II, pp. 325-333.
- 824 Dublyansky, Y., Moseley, G.E., Lyakhnitsky, Y., Cheng, H., Edwards, L.R., Scholz, D.,  
825 Koltai, G., Spötl, C., 2018. Late Palaeolithic cave art and permafrost in the  
826 Southern Ural. *Sci. Rep.* 8, 12080. <https://doi.org/10.1038/s41598-018-30049-w>
- 827 Fankhauser, A., McDermott, F., Fleitmann, D., 2016. Episodic speleothem deposition  
828 tracks the terrestrial impact of millennial-scale last glacial climate variability in SW  
829 Ireland. *Quat. Sci. Rev.* 152, 104–117.  
830 <https://doi.org/10.1016/j.quascirev.2016.09.019>
- 831 Feuillet, T., 2011. Statistical analyses of active patterned ground occurrence in the  
832 Taillon Massif (Pyrénées, France/Spain). *Permafrost Periglacial Processes* 22,  
833 228–238. <https://doi.org/10.1002/ppp.726>
- 834 García-Ruiz, J.M., Palacios, D., Andrés, N. de, Valero-Garcés, B.L., López-Moreno, J.I.,  
835 Sanjuán, Y., 2014. Holocene and 'Little Ice Age' glacial activity in the Marboré  
836 Cirque, Monte Perdido Massif, Central Spanish Pyrenees. *The Holocene* 24,  
837 1439–1452. <https://doi.org/10.1177/0959683614544053>
- 838 García-Ruiz, J.M., Palacios, D., Andrés, N., López-Moreno, J.I., 2020. Neoglaciation in  
839 the Spanish Pyrenees: a multiproxy challenge. *Mediterr. Geosci. Rev.* 2, 21–36.  
840 <https://doi.org/10.1007/s42990-020-00022-9>
- 841 Gázquez, F., Bauska, T.K., Comas-Bru, L., Ghaleb, B., Calaforra, J.-M., Hodell, D.A.,  
842 2020. The potential of gypsum speleothems for paleoclimatology: application to  
843 the Iberian Roman Humid Period. *Sci. Rep.* 10, 14705.  
844 <https://doi.org/10.1038/s41598-020-71679-3>
- 845 Gázquez, F., Calaforra, J.M., Evans, N.P., Hodell, D.A., 2017. Using stable isotopes  
846 ( $\delta^{17}\text{O}$ ,  $\delta^{18}\text{O}$  and  $\delta\text{D}$ ) of gypsum hydration water to ascertain the role of water  
847 condensation in the formation of subaerial gypsum speleothems. *Chem. Geol.*  
848 452, 34–46. <https://doi.org/10.1016/j.chemgeo.2017.01.021>
- 849 Gellatly, A.F., Grove, J.M., Switsur, V.R., 1992. Mid-Holocene glacial activity in the  
850 Pyrenees. *The Holocene* 2, 266–270.  
851 <https://doi.org/10.1177/095968369200200309>
- 852 Gomez Lende, M., Berenguer, F., Serrano, E., 2014. Morphology, ice types and thermal  
853 regime in a high mountain ice cave. First studies applying terrestrial laser scanner  
854 in the peña castil ice cave (Picos de Europa, Northern Spain). *Geogr. Fis. E Din.*  
855 *Quat.* 37, 141–150. <https://doi.org/10.4461/GFDQ.2014.37.13>
- 856 Gómez Lende, M., Serrano, E., Bordehore, L.J., Sandoval, S., 2016. The role of GPR  
857 techniques in determining ice cave properties: Peña Castil ice cave, Picos de  
858 Europa. *Earth Surf. Process. Landf.* 41, 2177–2190.  
859 <https://doi.org/10.1002/esp.3976>
- 860 Gómez-Ortiz, A., Oliva, M., Salvador-Franch, F., Palacios, D., Tanarro, L.M., de Sanjosé-  
861 Blasco, J.J., Salvà-Catarineu, M., 2019. Monitoring permafrost and periglacial  
862 processes in Sierra Nevada (Spain) from 2001 to 2016. *Permafrost Periglacial*  
863 *Processess* 30, 278–291. <https://doi.org/10.1002/ppp.2002>
- 864 González Trueba, J.J., Moreno, R.M., Martínez de Pisón, E., Serrano, E., 2008. 'Little  
865 Ice Age' glaciation and current glaciers in the Iberian Peninsula. *The Holocene*  
866 18, 551–568. <https://doi.org/10.1177/0959683608089209>
- 867 Gruber, S., Haeberli, W., 2009. Mountain permafrost, in: Margesin, R. (Ed.), *Permafrost*  
868 *Soils, Soil Biology*. Springer, Berlin, pp. 33–44. [https://doi.org/10.1007/978-3-540-69371-0\\_3](https://doi.org/10.1007/978-3-540-69371-0_3)
- 869
- 870 Gubler, S., Fiddes, J., Keller, M., Gruber, S., 2011. Scale-dependent measurement and  
871 analysis of ground surface temperature variability in alpine terrain. *The*  
872 *Cryosphere* 5, 431–443. <https://doi.org/10.5194/tc-5-431-2011>
- 873 Haeberli, W., Rellstab, W., Harrison, W.D., 1984. Geothermal effects of 18 ka BP ice  
874 conditions in the Swiss Plateau. *Ann. Glaciol.* 5, 56–60.  
875 <https://doi.org/10.3189/1984AoG5-1-56-60>



- 876 Harris, C., Vonder Mühll, D., Isaksen, K., Haeberli, W., Sollid, J.L., King, L., Holmlund,  
877 P., Dramis, F., Guglielmin, M., Palacios, D., 2003. Warming permafrost in  
878 European mountains. *Glob. Planet. Change* 39, 215–225.  
879 <https://doi.org/10.1016/j.gloplacha.2003.04.001>
- 880 Heeb, B., 2014. The next generation of the DistoX cave surveying instrument. *CREG J.*,  
881 88, 5-8.
- 882 Hill, C.A., 1987. Geology of Carlsbad Cavern and other caves in the Guadalupe  
883 Mountains, New Mexico and Texas. *Bull. 117 N. M. Bur. Mines Miner. Resour.*
- 884 Hock, R., Rasul, G., Adler, C., Cáceres, B., Gruber, S., Hirabayashi, Y., Jackson, J.,  
885 Kääb, A., Kang, S., Kutuzov, S., Milner, A., Molau, U., Morin, S., Orlove, B.,  
886 Steltzer, H., 2019. High Mountain Areas. In: *IPCC Special Report on the Ocean  
887 and Cryosphere in a Changing Climate.*
- 888 Kern, Z., Bočić, N., Sipos, G., 2018. Radiocarbon-dated vegetal remains from the cave  
889 ice deposits of Velebit Mountain, Croatia. *Radiocarbon* 60, 1391–1402.  
890 <https://doi.org/10.1017/RDC.2018.108>
- 891 Kern, Z., Perşoiu, A., 2013. Cave ice – the imminent loss of untapped mid-latitude  
892 cryospheric palaeoenvironmental archives. *Quat. Sci. Rev.* 67, 1–7.  
893 <https://doi.org/10.1016/j.quascirev.2013.01.008>
- 894 Koltai, G., Spötl, C., Jarosch, A.H., Cheng, H., 2020. Cryogenic cave carbonates in the  
895 Dolomites (Northern Italy): insights into Younger Dryas cooling and seasonal  
896 precipitation. *Clim. Past.* 17, 775–789.
- 897 Korshunov, V.V., Shavrina, E.V., 1998. Gypsum speleothems of freezing origin. *J. Cave  
898 Karst Stud.* 60, 146–150.
- 899 Lechleitner, F.A., Mason, A.J., Breitenbach, S.F.M., Vaks, A., Haghipour, N., Henderson,  
900 G.M., 2020. Permafrost-related hiatuses in stalagmites: Evaluating the potential  
901 for reconstruction of carbon cycle dynamics. *Quat. Geochronol.* 56, 101037.  
902 <https://doi.org/10.1016/j.quageo.2019.101037>
- 903 Leunda, M., González-Sampériz, P., Gil-Romera, G., Bartolomé, M., Belmonte-Ribas,  
904 Á., Gómez-García, D., Kaltenrieder, P., Rubiales, J.M., Schwörer, C., Tinner, W.,  
905 Morales-Molino, C., Sancho, C., 2019. Ice cave reveals environmental forcing of  
906 long-term Pyrenean tree line dynamics. *J. Ecol.* 107, 814–828.  
907 <https://doi.org/10.1111/1365-2745.13077>
- 908 Lewkowicz, A.G., Ednie, M., 2004. Probability mapping of mountain permafrost using the  
909 BTS method, Wolf Creek, Yukon Territory, Canada. *Permafrost Periglacial  
910 Processes* 15, 67–80. <https://doi.org/10.1002/ppp.480>
- 911 López-Moreno, J.I., Alonso-González, E., Monserrat, O., Del Río, L.M., Otero, J.,  
912 Lapazaran, J., Luzi, G., Dematteis, N., Serreta, A., Rico, I., Serrano-Cañadas, E.,  
913 Bartolomé, M., Moreno, A., Buisan, S., Revuelto, J., 2019. Ground-based remote-  
914 sensing techniques for diagnosis of the current state and recent evolution of the  
915 Monte Perdido Glacier, Spanish Pyrenees. *J. Glaciol.* 65, 85–100.  
916 <https://doi.org/10.1017/jog.2018.96>
- 917 López-Moreno, J.I., Revuelto, J., Rico, I., Chueca-Cía, J., Julián, A., Serreta, A., Serrano,  
918 E., Vicente-Serrano, S.M., Azorin-Molina, C., Alonso-González, E., García-Ruiz,  
919 J.M., 2016. Thinning of the Monte Perdido Glacier in the Spanish Pyrenees since  
920 1981. *The Cryosphere* 10, 681–694. <https://doi.org/10.5194/tc-10-681-2016>
- 921 Losiak, A., Derkowski, A., Skąła, A., Trzciński, J., 2016. Evaporites on ice: how to form  
922 gypsum on Antarctica and on Martian North polar residual cap? In: *47th Lunar and  
923 Planetary Science Conference.* 1972.pdf.
- 924 Luetscher, M., Bolius, D., Schwikowski, M., Schotterer, U., Smart, P.L., 2007.  
925 Comparison of techniques for dating of subsurface ice from Monlesi ice cave,  
926 Switzerland. *J. Glaciol.* 53, 374–384.
- 927 Luetscher, M., Borreguero, M., Moseley, G.E., Spötl, C., Edwards, R.L., 2013. Alpine  
928 permafrost thawing during the Medieval Warm Period identified from cryogenic  
929 cave carbonates. *The Cryosphere* 7, 1073–1081. [https://doi.org/10.5194/tc-7-  
930 1073-2013](https://doi.org/10.5194/tc-7-1073-2013)



- 931 Luetscher, M., Jeannin, P.-Y., 2018. Ice Caves in Switzerland, in: Perşoiu, A., Lauritzen,  
932 S.-E. (Eds.), *Ice Caves*. Elsevier, pp. 221–235. <https://doi.org/10.1016/B978-0->  
933 12-811739-2.00010-3
- 934 Luetscher, M., Lismonde, B., Jeannin, P.-Y., 2008. Heat exchanges in the heterothermic  
935 zone of a karst system: Monlesi cave, Swiss Jura Mountains. *J. Geophys. Res.*  
936 *Earth Surf.* 113. <https://doi.org/10.1029/2007JF000892>
- 937 Lundberg, J., McFarlane, D.A., 2007. Pleistocene depositional history in a periglacial  
938 terrane: A 500 k.y. record from Kents Cavern, Devon, United Kingdom.  
939 *Geosphere* 3, 199–219. <https://doi.org/10.1130/GES00085.1>
- 940 Marshall, P., Brown, M.C., 1974. Ice in Coulthard Cave, Alberta. *Can. J. Earth Sci.*  
941 <https://doi.org/10.1139/e74-045>
- 942 Mavlyudov, B.R., 2008. *Caves Glaciation in the Past*. Федеральное государственное  
943 бюджетное учреждение науки Институт географии Российской академии  
944 наук, pp. 499–505.
- 945 Moseley, G.E., Edwards, R.L., Lord, N.S., Spötl, C., Cheng, H., 2021. Speleothem record  
946 of mild and wet mid-Pleistocene climate in northeast Greenland. *Sci. Adv.* 7,  
947 eabe1260. <https://doi.org/10.1126/sciadv.abe1260>
- 948 Munroe, J.S., 2021. First investigation of perennial ice in Winter Wonderland Cave, Uinta  
949 Mountains, Utah, USA. *The Cryosphere* 15, 863–881. <https://doi.org/10.5194/tc->  
950 15-863-2021
- 951 Munroe, J., Kimble, K., Spötl, C., Marks, G.S., McGee, D., Herron, D., 2021. Cryogenic  
952 cave carbonate and implications for thawing permafrost at Winter Wonderland  
953 Cave, Utah, USA. *Sci. Rep.* 11, 6430. <https://doi.org/10.1038/s41598-021->  
954 85658-9
- 955 Navarro-Serrano, F., López-Moreno, J.I., Azorin-Molina, C., Alonso-González, E.,  
956 Tomás-Burguera, M., Sanmiguel-Valladolid, A., Revuelto, J., Vicente-Serrano,  
957 S.M., 2018. Estimation of near-surface air temperature lapse rates over  
958 continental Spain and its mountain areas. *Int. J. Climatol.* 38, 3233–3249.  
959 <https://doi.org/10.1002/joc.5497>
- 960 Noetzi, J., Gruber, S., 2009. Transient thermal effects in Alpine permafrost. *The*  
961 *Cryosphere* 3, 85–99. <https://doi.org/10.5194/tc-3-85-2009>
- 962 Orvošová, M., Deininger, M., Milovský, R., 2014. Permafrost occurrence during the Last  
963 Permafrost Maximum in the Western Carpathian Mountains of Slovakia as  
964 inferred from cryogenic cave carbonate. *Boreas* 43, 750–758.  
965 <https://doi.org/10.1111/bor.12042>
- 966 Perşoiu, A., Buzjak, N., Onaca, A., Pennos, C., Sotiriadis, Y., Ionita, M., Zachariadis, S.,  
967 Styllas, M., Kosutnik, J., Hegyi, A., Butorac, V., 2021. Record summer rains in  
968 2019 led to massive loss of surface and cave ice in SE Europe. *The Cryosphere*  
969 15, 2383–2399. <https://doi.org/10.5194/tc-15-2383-2021>
- 970 Perşoiu, A., Lauritzen, S.-E. (Eds.), 2018. *Ice caves*. Elsevier, Amsterdam.
- 971 Perşoiu, A., Onac, B.P., Wynn, J.G., Blaauw, M., Ionita, M., Hansson, M., 2017.  
972 Holocene winter climate variability in Central and Eastern Europe. *Sci. Rep.* 7,  
973 1196. <https://doi.org/10.1038/s41598-017-01397-w>
- 974 Pons, X., Ninyerola, M., 2008. Mapping a topographic global solar radiation model  
975 implemented in a GIS and refined with ground data. *Int. J. Climatol.* 28, 1821–  
976 1834. <https://doi.org/10.1002/joc.1676>
- 977 Racine, T.M.F., Spötl, C., Reimer, P.J., Čarga, J., 2022. Radiocarbon constraints on  
978 periods of positive cave ice mass balance during the last millennium, Julian Alps  
979 (NW Slovenia). *Radiocarbon* 1–24. <https://doi.org/10.1017/RDC.2022.26>
- 980 Reille, M., Andrieu, V., 1995. The late Pleistocene and Holocene in the Lourdes Basin,  
981 Western Pyrénées, France: new pollen analytical and chronological data. *Veg.*  
982 *Hist. Archaeobotany* 4, 1–21. <https://doi.org/10.1007/BF00198611>
- 983 Requirand, C., 2014. Hypothèse sur la formation des cristaux de gypse Grotte Glacée  
984 Devaux (Gavarnie - Hautes Pyrénées). *Bulletin de la Société Ramon.* 11 pp.



- 985 Richter, D.K., Meissner, P., Immenhauser, A., Schulte, U., Dorsten, I., 2010. Cryogenic  
986 and non-cryogenic pool calcites indicating permafrost and non-permafrost  
987 periods: a case study from the Herbstlabyrinth-Advent Cave system (Germany).  
988 *The Cryosphere* 4, 501–509. <https://doi.org/10.5194/tc-4-501-2010>
- 989 Rico, I., Magnin, F., López Moreno, J.I., Serrano, E., Alonso-González, E., Revuelto, J.,  
990 Hughes-Allen, L., Gómez-Lende, M., 2021. First evidence of rock wall permafrost  
991 in the Pyrenees (Vignemale peak, 3,298 m a.s.l., 42°46'16"N/0°08'33"W).  
992 *Permafrost Periglacial Processes* 32, 673–680. <https://doi.org/10.1002/ppp.2130>
- 993 Rösch, G., Rösch, J., 1935. Visites à la grotte Devaux. *La Montagne. Revue du Club*  
994 *Alpin Français*, N° 269, pp.171-178.
- 995 Rösch, J., 1949. Une exploration de la Grotte Devaux à Gavarnie. *Bulletin de la section*  
996 *du Sud-Ouest de la Club Alpin Français*, N°69. pp. 103-107.
- 997 Sancho, C., Belmonte, Á., Bartolomé, M., Moreno, A., Leunda, M., López-Martínez, J.,  
998 2018a. Middle-to-late Holocene palaeoenvironmental reconstruction from the  
999 A294 ice-cave record (Central Pyrenees, northern Spain). *Earth Planet. Sci. Lett.*  
1000 484, 135–144. <https://doi.org/10.1016/j.epsl.2017.12.027>
- 1001 Sancho, C., Arenas, C., Pardo, G., Peña-Monné, J.L., Rhodes, E.J., Bartolomé, M.,  
1002 García-Ruiz, J.M., Martí-Bono, C., 2018b. Glaciolacustrine deposits formed in an  
1003 ice-dammed tributary valley in the south-central Pyrenees: New evidence for late  
1004 Pleistocene climate. *Sedim. Geol.* 366, 47–66.  
1005 <https://doi.org/10.1016/j.sedgeo.2018.01.008>
- 1006 Sancho, C., Peña, J.L., Mikkan, R., Osácar, C., Quinif, Y., 2004. Morphological and  
1007 speleothemic development in Brujas Cave (Southern Andean Range, Argentine):  
1008 palaeoenvironmental significance. *Geomorphology* 57, 367–384.  
1009 [https://doi.org/10.1016/S0169-555X\(03\)00166-1](https://doi.org/10.1016/S0169-555X(03)00166-1)
- 1010 Scandroglio, R., Draebing, D., Offer, M., Krautblatter, M., 2021. 4D quantification of  
1011 alpine permafrost degradation in steep rock walls using a laboratory-calibrated  
1012 electrical resistivity tomography approach. *Surf. Geophys.* 19, 241–260.  
1013 <https://doi.org/10.1002/nsg.12149>
- 1014 Seal, R.R., II, 2006. Sulfur isotope geochemistry of sulfide minerals. *Rev. Mineral.*  
1015 *Geochem.* 61, 633–677. <https://doi.org/10.2138/rmg.2006.61.12>
- 1016 Serrano, E., Gómez-Lende, M., Belmonte, Á., Sancho, C., Sánchez-Benítez, J.,  
1017 Bartolomé, M., Leunda, M., Moreno, A., Hivert, B., 2018. Ice Caves in Spain, in:  
1018 Perşoiu, A., Lauritzen, S.-E. (Eds.), *Ice Caves*. Elsevier, pp. 625–655.  
1019 <https://doi.org/10.1016/B978-0-12-811739-2.00028-0>
- 1020 Serrano, E., López-Moreno, J.I., Gómez-Lende, M., Pisabarro, A., Martín-Moreno, R.,  
1021 Rico, I., Alonso-González, E., 2020. Frozen ground and periglacial processes  
1022 relationship in temperate high mountains: a case study at Monte Perdido-  
1023 Tucarroya area (The Pyrenees, Spain). *J. Mt. Sci.* 17, 1013–1031.  
1024 <https://doi.org/10.1007/s11629-019-5614-5>
- 1025 Serrano, E., Sanjosé-Blasco, J.J. de, Gómez-Lende, M., López-Moreno, J.I., Pisabarro,  
1026 A., Martínez-Fernández, A., 2019. Periglacial environments and frozen ground in  
1027 the central Pyrenean high mountain area: Ground thermal regime and distribution  
1028 of landforms and processes. *Permafrost Periglacial Processes* 30, 292–309.  
1029 <https://doi.org/10.1002/ppp.2032>
- 1030 Spötl, C., Cheng, H., 2014. Holocene climate change, permafrost and cryogenic  
1031 carbonate formation: insights from a recently deglaciated, high-elevation cave in  
1032 the Austrian Alps. *Clim. Past* 10, 1349–1362. <https://doi.org/10.5194/cp-10-1349-2014>
- 1033  
1034 Spötl, C., Reimer, P.J., Luetscher, M., 2013. Long-term mass balance of perennial firn  
1035 and ice in an Alpine cave (Austria): Constraints from radiocarbon-dated wood  
1036 fragments. *The Holocene* 0959683613515729.  
1037 <https://doi.org/10.1177/0959683613515729>
- 1038 Stoffel, M., Luetscher, M., Bollschweiler, M., Schlatter, F., 2009. Evidence of NAO control  
1039 on subsurface ice accumulation in a 1200 yr old cave-ice sequence, St. Livres



- 1040 ice cave, Switzerland. *Quat. Res.* 72, 16–26.  
1041 <https://doi.org/10.1016/j.yqres.2009.03.002>
- 1042 Supper, R., Ottowitz, D., Jochum, B., Römer, A., Pfeiler, S., Kauer, S., Keuschnig, M.,  
1043 Ita, A., 2014. Geoelectrical monitoring of frozen ground and permafrost in alpine  
1044 areas: field studies and considerations towards an improved measuring  
1045 technology. *Surf. Geophys.* 12, 93–115. [https://doi.org/10.3997/1873-](https://doi.org/10.3997/1873-0604.2013057)  
1046 [0604.2013057](https://doi.org/10.3997/1873-0604.2013057)
- 1047 Temovski, M., Futó, I., Túri, M., Palcsu, L., 2018. Sulfur and oxygen isotopes in the  
1048 gypsum deposits of the Provalata sulfuric acid cave (Macedonia).  
1049 *Geomorphology* 315, 80–90. <https://doi.org/10.1016/j.geomorph.2018.05.010>
- 1050 Vaks, A., Gutareva, O.S., Breitenbach, S.F.M., Avirmed, E., Mason, A.J., Thomas, A.L.,  
1051 Osinzev, A.V., Kononov, A.M., Henderson, G.M., 2013. Speleothems Reveal  
1052 500,000-Year History of Siberian Permafrost. *Science* 340, 183–186.  
1053 <https://doi.org/10.1126/science.1228729>
- 1054 Vaks, A., Mason, A.J., Breitenbach, S.F.M., Kononov, A.M., Osinzev, A.V., Rosensaft,  
1055 M., Borshevsky, A., Gutareva, O.S., Henderson, G.M., 2020. Palaeoclimate  
1056 evidence of vulnerable permafrost during times of low sea ice. *Nature* 577, 221–  
1057 225. <https://doi.org/10.1038/s41586-019-1880-1>
- 1058 Wind, M., Obleitner, F., Racine, T., Spötl, C., 2022. Multi-annual temperature evolution  
1059 and implications for cave ice development in a sag-type ice cave in the Austrian  
1060 Alps. *Cryosphere Discuss.* 1–26. <https://doi.org/10.5194/tc-2022-67>
- 1061 Wollenburg, J.E., Katlein, C., Nehrke, G., Nöthig, E.-M., Matthiessen, J., Wolf- Gladrow,  
1062 D.A., Nikolopoulos, A., Gázquez-Sanchez, F., Rossmann, L., Assmy, P., Babin,  
1063 M., Bruyant, F., Beaulieu, M., Dybwad, C., Peeken, I., 2018. Ballasting by  
1064 cryogenic gypsum enhances carbon export in a Phaeocystis under-ice bloom.  
1065 *Sci. Rep.* 8, 7703. <https://doi.org/10.1038/s41598-018-26016-0>
- 1066 Yonge, C.J., Ford, D., Horne, G., Lauriol, B., Schroeder, J., 2018. Ice Caves in Canada,  
1067 in: Perşoiu, A., Lauritzen, S.-E. (Eds.), *Ice Caves*. Elsevier, pp. 285–334.  
1068 <https://doi.org/10.1016/B978-0-12-811739-2.00015-2>
- 1069 Žák, K., Onac, B.P., Kadebskaya, O.I., Filippi, M., Dublyansky, Y., Luetscher, M., 2018.  
1070 Cryogenic mineral formation in caves, in: Perşoiu, A., Lauritzen, S.-E. (Eds.), *Ice*  
1071 *Caves*. Elsevier, pp. 123–162. [https://doi.org/10.1016/B978-0-12-811739-](https://doi.org/10.1016/B978-0-12-811739-2.00035-8)  
1072 [2.00035-8](https://doi.org/10.1016/B978-0-12-811739-2.00035-8)
- 1073 Žák, K., Richter, D.K., Filippi, M., Živor, R., Deininger, M., Mangini, A., Scholz, D., 2012.  
1074 Coarsely crystalline cryogenic cave carbonate &ndash; a new archive to estimate  
1075 the Last Glacial minimum permafrost depth in Central Europe. *Clim. Past* 8,  
1076 1821–1837. <https://doi.org/10.5194/cp-8-1821-2012>
- 1077 Žák, K., Urban, J., Čílek, V., Hercman, H., 2004. Cryogenic cave calcite from several  
1078 Central European caves: age, carbon and oxygen isotopes and a genetic model.  
1079 *Chem. Geol.* 206, 119–136. <https://doi.org/10.1016/j.chemgeo.2004.01.012>
- 1080 Zerkle, A.L., Jones, D.S., Farquhar, J., Macalady, J.L., 2016. Sulfur isotope values in the  
1081 sulfidic Frasassi cave system, central Italy: A case study of a chemolithotrophic  
1082 S-based ecosystem. *Geochim. Cosmochim. Acta* 173, 373–386.  
1083 <https://doi.org/10.1016/j.gca.2015.10.028>  
1084



Figure 1. (a) Location of Devaux cave in the Central Pyrenees (ASTER GDEM, NASA v3, 2019). (b) Satellite image and location of Devaux cave, main peaks, lakes, glaciers and cirques in the study area (3D ©Google Earth). The yellow arrows indicate the underground flow path from Lago helado to the Gavarnie waterfall according to the dye-tracing experiment of [du Cailar et al. \(1953\)](#). (c) View towards the entrances of Devaux cave. The lower entrance (~2821 m a.s.l.) corresponds to the Brulle spring (Spring North 1), while the upper one corresponds to the main entrance (Porche (South), ~2836 m a.s.l.). Spring North 2 is located between both entrances. Note person for scale (within the white circle). Remnants of ice partially blocking Brulle and Spring North 2 (July 2021). (d) Landscape view of the catchment area and approximate location of Devaux cave (in dark pink; photo: Paul Cluzon). (e) Ponor located on the southern shore of Lago Helado.

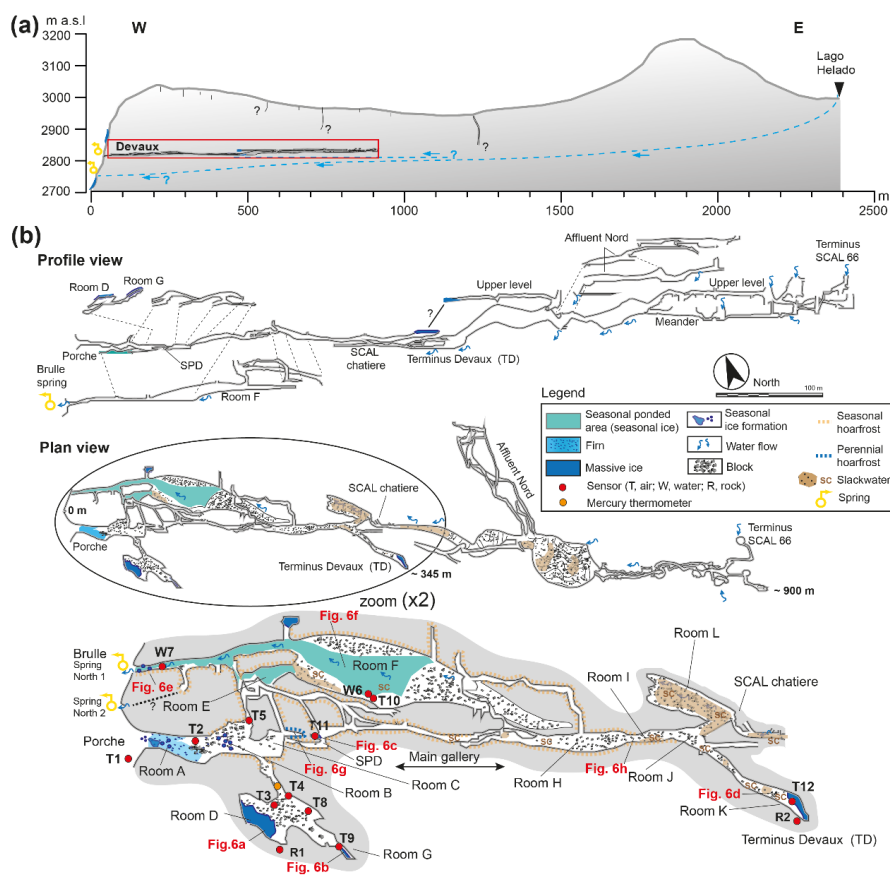


Figure 2. (a) Schematic W-E cross section from Lago helado to Devaux cave and the interpreted underground flow path according to [du Cailar et al. \(1953\)](#). (b) Longitudinal section and plan view of Devaux cave showing the location of sensors and cave deposits. Labels R, W and T refer to rock, water and air temperature sensors, respectively. The enlarged area corresponds to the first ~345 m of the studied sector. Red labels correspond to the approximate location of the photographs in Fig. 7. Cave survey by Marc Galy, Groupe Spéléologique des Pyrénées (GSPY 86).

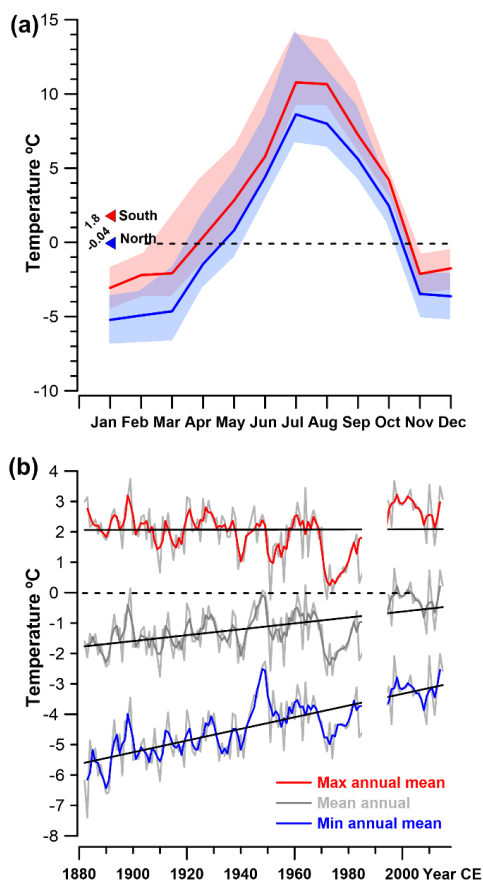


Figure 3. (a) Monthly temperature variation on the northern and southern side of the Monte Perdido massif. Red and blue triangles correspond to the 4-year means. The dashed black line indicates 0°C. Light red and blue shaded envelopes represent the maximum and minimum mean monthly temperatures, respectively. (b) Maximum, mean and minimum annual temperatures recorded at the Pic du Midi de Bigorre station since 1882. Black line indicates the general trend and dashed black line corresponds to 0°C.

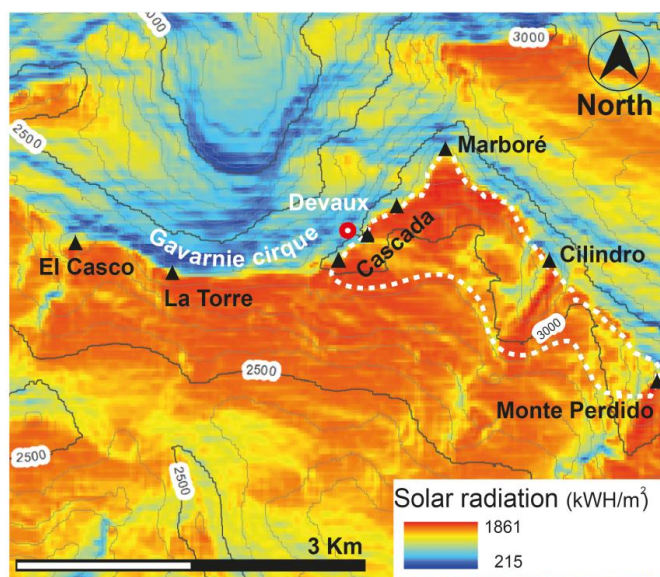


Figure 4. Solar radiation map of the study area. The solar radiation anomaly observed in the Gavarnie cirque is explained by its northerly orientation and the cirque morphology. Black triangles indicate the main peaks above 3000 m. The red-white circle marks Devaux cave, while the dashed white line delineates the approximate catchment.

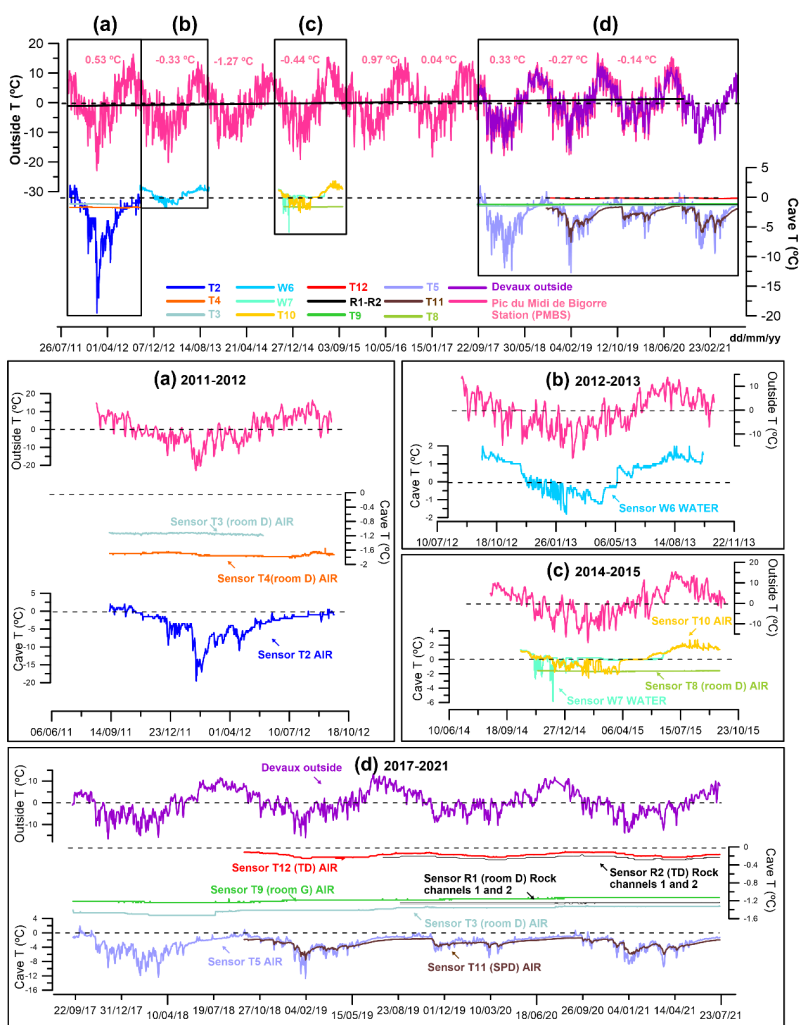


Figure 5. Mean daily air temperature variations at the Pic du Midi de Bigorre station (2860 m a.s.l., red), daily outside air temperature at Devaux cave (2836 m a.s.l., purple) and temperature variations in air, water and rock in the cave for the different time windows since 2011. Dark pink numbers are mean annual air temperatures (MAAT) at the Pic du Midi de Bigorre station (PMBS). Dashed lines indicate 0 °C. Black squares labelled a, b, c, and d correspond to the areas enlarged below. The black continuous line is the external temperature trend during the monitoring period.

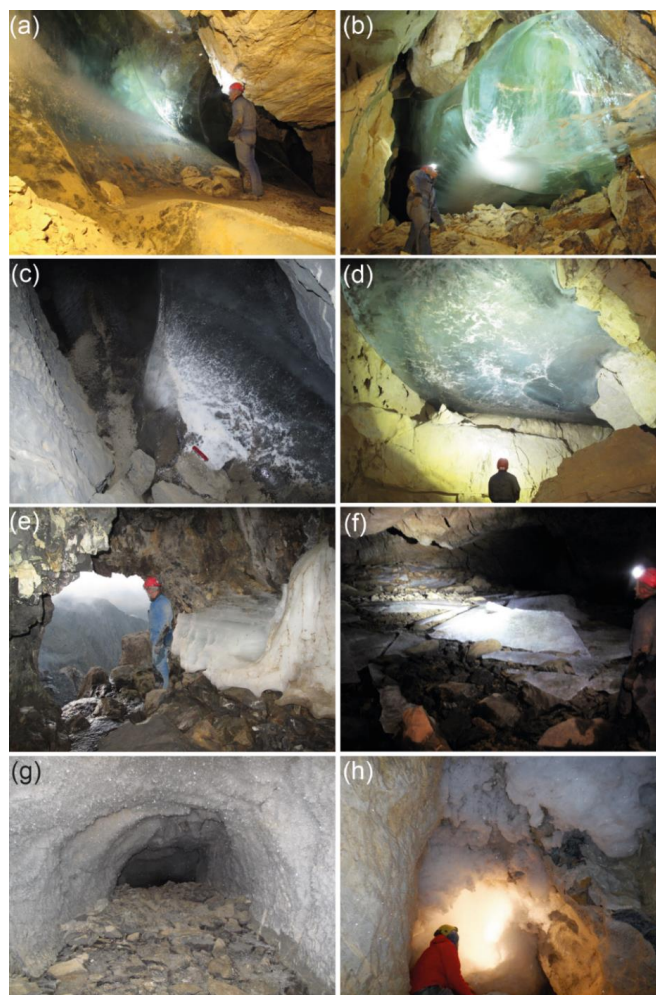


Figure 6. (a) Upper part of the ice body in room D. (b) Ice body hanging from the ceiling and the southwest wall in room G. White colours at the bottom of the deposit correspond to the concentration of air inclusions as well as cryogenic carbonates and gypsum in the ice. (c) Small ice body in room SPD with CCC-CCG on and within the ice. Red knife (9 cm) for scale. (d) Ice body on the ceiling of room K (Terminus Devaux, TD). (e) Brulle spring and remains of a layered ice body (September 2018). (f) Broken ice sheets in the flooded area in room F (September 2018). (g) Millimetre to centimetre size perennial hoarfrost in a blind gallery below SPD room. (h) Seasonal hoarfrost aggregates (>30 cm long size) covering a cupola close to room J.

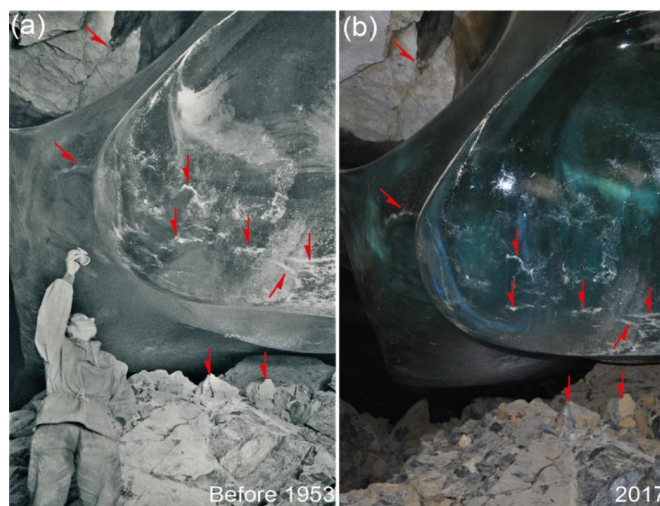


Figure 7. (a) Photo of the ice body located in room G before 1953 (Casteret, 1953). (b) Photo taken in 2017. In both pictures, white patches on the ice surface correspond to small CCC accumulations released from the ice by sublimation. Red arrows indicate common features in both images.

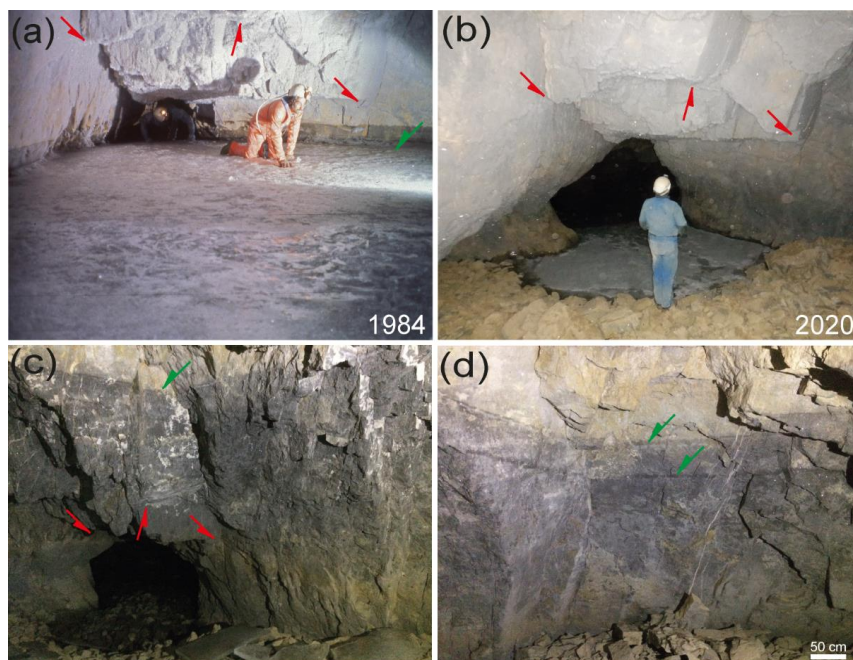


Figure 8. (a) Photo taken close to the river sector that connects the rooms F and E. The estimated ice level is 5 m higher than the Brulle spring. Photo by Jean Luc Bernardin (8<sup>th</sup> August 1984). (b) Similar area in 2020, and maximum extension of the seasonal lake ice formed during winter. (c) Higher ice mark level (c. +9.5 m with respect to the Brulle spring) and remnants of ice sheets from the frozen lake in 2018. (d) Two ice level marks (c. +9.2 m and +8.8 m with respect to the Brulle spring) located between the highest mark and the elevation of the ice in photo (a). In all images red arrows indicate the same rock edges, while green arrows show ice-level marks.

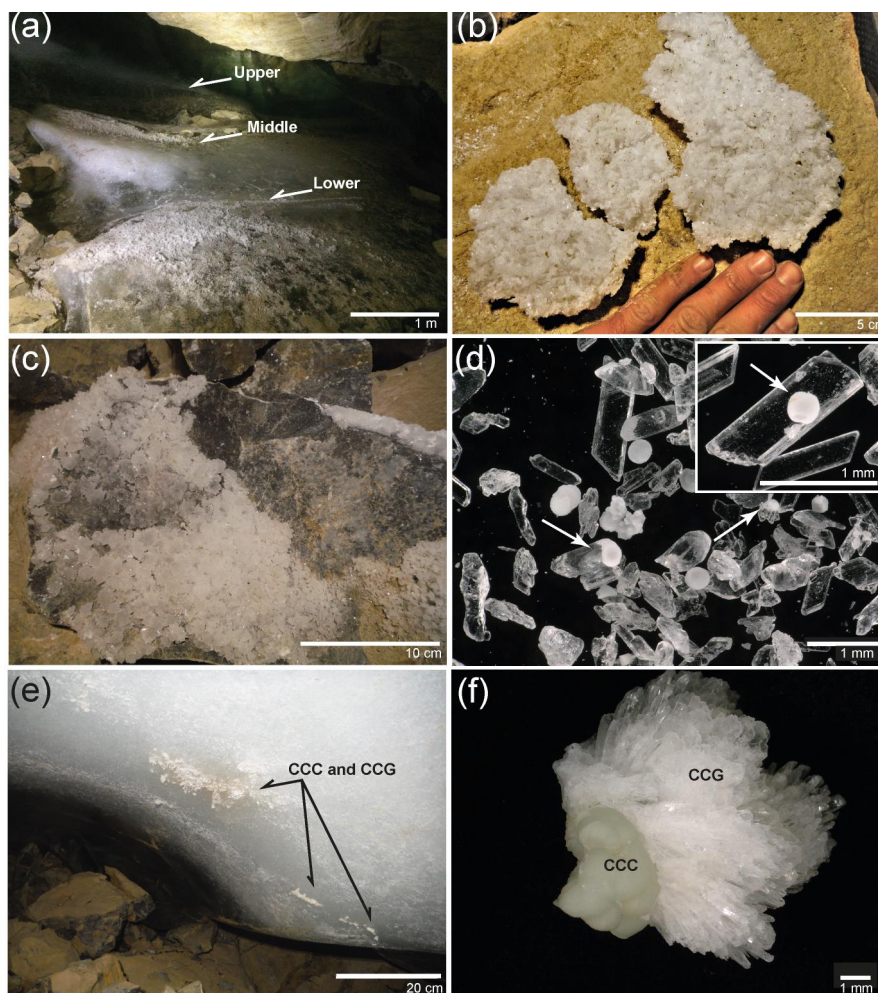


Figure 9. (a) Ice body in room G and three levels marked by cryogenic gypsum partially still in situ in the ice. The whitest area corresponds to milky ice with a high abundance of air inclusions. Gypsum crystals cover parts of the surface of the ice body due to ice retreat. (b) Large gypsum “raft” deposited on a block in room D. (c) Block in room D with gypsum overgrowths. (d) Microscopic image of euhedral CCG with local cores of CCC (white arrows), globular CCC, and detail of euhedral gypsum crystal with a core of globular CCC. (e) CCC and CCG entrapped within milky ice in room G. (f) Detail of a CCC sample from room G covered by CCG.



Date	Sample	Cations					Anions									
		Na <sup>+</sup>	NH <sub>4</sub> <sup>+</sup>	K <sup>+</sup>	Ca <sup>2+</sup>	Mg <sup>2+</sup>	F <sup>-</sup>	Cl <sup>-</sup>	NO <sub>2</sub> <sup>-</sup>	Br <sup>-</sup>	NO <sub>3</sub> <sup>-</sup>	SO <sub>4</sub> <sup>2-</sup>	HCO <sub>3</sub> <sup>-</sup>	CO <sub>3</sub> <sup>2-</sup>	PO <sub>4</sub> <sup>3-</sup>	
15/09/2017	Devaux river 1	1.6	0.0	0.5	36.0	8.5	0.0	0.2	0.0	0.0	1.8	21.6	61.0	11.6	0.0	
	Devaux drip 1	0.9	0.1	0.5	50.5	18.2	0.1	0.5	0.0	0.0	6.8	67.4	95.2	0.0	0.0	
	Devaux drip 2	1.4	1.2	1.3	53.2	19.5	0.1	1.1	0.1	0.0	7.4	70.1	101.3	0.0	0.0	
22/07/2018	Devaux Ice 1 (room D)	2.3	0.0	0.3	24.8	2.7	0.1	1.3	0.0	0.0	0.7	19.0	23.9	1.0	0.0	
	Devaux Ice 2 (room D)	2.2	1.3	2.5	27.8	2.0	0.0	2.1	0.0	0.0	1.5	17.0	30.7	0.0	0.0	
	Devaux river 1	0.6	0.0	0.4	32.4	4.4	0.0	0.2	0.0	0.0	0.9	5.1	53.7	4.0	0.1	
	Devaux river 2	0.6	0.0	0.4	32.2	4.4	0.0	0.2	0.0	0.0	0.9	5.1	56.1	2.6	0.0	
	Devaux drip 1	1.4	0.0	3.2	61.0	20.8	0.2	2.2	0.0	0.0	14.1	76.0	84.2	5.6	0.0	
22/09/2018	Devaux drip 2	2.3	0.1	1.7	60.8	21.0	0.2	2.2	0.0	0.0	14.1	76.9	91.5	4.4	0.0	
	Devaux river 1*	1.3	0.0	0.4	40.5	7.9	0.0	0.3	0.0	0.0	2.0	17.0	65.9	0.0	0.0	
	Devaux drip 1*	1.6	0.0	1.2	70.6	27.2	0.2	1.1	0.0	0.0	19.8	116.5	90.3	0.0	0.0	
28/07/2020	Devaux ice (seasonal)*	0.4	0.0	0.5	28.2	1.1	0.1	0.5	0.0	0.0	0.5	2.8	36.6	0.0	0.0	
	Devaux river 1*	0.6	0.0	0.3	31.5	4.1	0.0	0.2	0.0	0.0	0.8	5.9	58.6	0.0	0.0	
	Devaux drip 1*	1.1	0.2	1.1	42.3	12.5	0.1	0.5	0.0	0.0	2.9	38.4	101.3	0.0	0.0	
	Devaux drip 2*	1.1	0.1	1.0	43.6	13.5	0.1	0.4	0.0	0.0	2.7	38.2	89.1	0.0	0.0	
	Devaux drip 3*	1.6	0.7	1.5	47.9	13.1	0.1	1.1	0.0	0.0	2.2	36.7	107.4	0.0	0.0	
26/07/2021	Devaux drip 1	2.9	0.0	1.1	83	35.9	0.3	5.9	0.6	0.1	40.2	269.3	104.9	0.0	0.0	
	Devaux drip 2	3.3	0.4	2.0	73.2	29.3	0.2	6.0	0.1	0.0	28.6	212	112.2	0.0	0.0	
	Devaux river 1	0.4	0.0	0.1	25.7	4.3	0.1	2.6	0.1	0.0	3.2	16.3	68.3	0.0	0.0	
13/08/2021	Devaux river 1	0.7	0.0	0.2	28.6	4.9	0.1	2.6	0.0	0.0	1.5	20.4	74.4	0.0	0.0	
	Devaux drip 1	7.5	2.2	5.1	49.5	15.2	0.2	10.3	0.3	0.0	6.9	77.3	130.5	0.0	0.0	
	Devaux drip 2	5.1	1.3	2.8	49.3	15.6	0.2	6.5	0.1	0.0	6.5	80.5	129.3	0.0	0.0	

Table 1. Chemical composition of water and ice samples from Devaux cave (in mg/l). \* Samples where TDS (total dissolved solids) was calculated.



Location	Sample and description	$\delta^{34}\text{S}$ (‰) VCDT
Room D	Gypsum crystal (part of large raft)	-15.8
Room D	Gypsum crystal (part of large raft)	-15.5
Room D; lower gypsum level	Gypsum crystal (individual)	-15.6
Room D; middle gypsum level	Gypsum crystal (individual)	-15.0
Room D; middle gypsum level	Gypsum crystal (individual)	-15.6
Room D; upper gypsum level	Tiny gypsum crystals (aliquot)	-15.3
Room D	Gypsum crystal (individual)	-15.1
Room G	Gypsum crystal (individual)	-12.3
Room G	Gypsum overgrowth (individual)	-12.1
Room G	Gypsum overgrowth (individual)	-11.9
Room G	Gypsum overgrowth (individual)	-12.1
Room G	Gypsum overgrowth (individual)	-12.0
Limestone above cave	Pyrite crystal (individual)	-12.7
Entrance "Porche"	Drip water (1 liter)	-14.4
Brulle spring	River water 1 (1 liter)	-28.5
Brulle spring	River water 2 (1 liter)	-27.3

Table 2. Sulfur isotope values of gypsum, water and pyrite from Devaux.